Synthesis, characterization, and environmental impact analysis of one-part alkali-activated materials based on alkali-fused basic oxygen furnace slag

Yang, Xinkui; Wu, Shaopeng; Xu, Shi; Liu, Chen; Chen, Boyu; Chen, Dongyu; Yang, Chao

DOI
10.1016/j.conbuildmat.2025.142514

Publication date
2025

Document Version
Final published version

Published in
Construction and Building Materials

Citation (APA)
Yang, X., Wu, S., Xu, S., Liu, C., Chen, B., Chen, D., & Yang, C. (2025). Synthesis, characterization, and environmental impact analysis of one-part alkali-activated materials based on alkali-fused basic oxygen furnace slag. *Construction and Building Materials*, *490*, Article 142514. https://doi.org/10.1016/j.conbuildmat.2025.142514

Construction and Building Materials 490 (2025) 142514

Contents lists available at ScienceDirect

Construction and Building Materials

journal homepage: www.elsevier.com/locate/conbuildmat

Synthesis, characterization, and environmental impact analysis of one-part alkali-activated materials based on alkali-fused basic oxygen furnace slag

Xinkui Yang [a], Shaopeng Wu [a], Shi Xu [b,c,*], Chen Liu [c], Boyu Chen [c], Dongyu Chen [a], Chao Yang [d]

[a] State Key Laboratory of Silicate Materials for Architectures, Wuhan University of Technology, Wuhan 430070, China
[b] School of Civil Engineering and Architecture, Wuhan University of Technology, Luoshi Road 122, Wuhan 430070, China
[c] Faculty of Civil Engineering and Geosciences, Delft University of Technology, Stevinweg 1, Delft 2628 CN, the Netherlands
[d] School of Civil Engineering, Architecture and Environment, Hubei University of Technology, Wuhan 430068, China

ARTICLE INFO

Keywords:
Basic oxygen furnace slag
Alkali fusion
One-part alkali-activated materials
Reaction products
Compressive strength
Life cycle assessment

ABSTRACT

One-part alkali-activated materials (AAM), a low-carbon alternative to cement, can reduce CO_2 emissions while improving the utilization of industrial by-products. In this study, basic oxygen furnace slag (BOFS) was activated by alkali fusion with different contents of sodium hydroxide (NaOH), and the optimum NaOH content was selected by the mineral phase composition and micromorphology of alkali-fused basic oxygen furnace slag (ABOFS). Then, ABOFS and ground granular blast furnace slag (GGBFS) were used to prepare one-part AAM pastes, and the effects of GGBFS content on the reaction products, microstructure, leaching characteristics and mechanical strength of one-part AAM pastes were studied. Finally, the life cycle assessment (LCA) of one-part AAM pastes was conducted. The results showed that alkali fusion activation promoted the formation of reactive mineral phases in BOFS and increased its specific surface area. The optimum NaOH content for alkali fusion activation is 10 wt%. The reaction products of one-part AAM pastes primarily consisted of C-(N-)A-S-H gel and hydrotalcite. As GGBFS content increased from 0 wt% to 80 wt%, the amount of gel products first increased and then decreased, peaking at 60 wt%. The addition of GGBFS reduced the porosity of pastes and increased the proportion of gel pores, resulting in a denser structure. Therefore, the compressive strength of one-part AAM pastes increased with the increase of GGBFS. LCA results indicate that the global warming potential (GWP) of one-part AAM is significantly lower than that of ordinary Portland cement. The findings of this study provide new insights into the application of BOFS in AAM.

1. Introduction

Steel slag is an industrial by-product generated during steelmaking. In 2023, China's crude steel production exceeds 1.02 billion tons, producing approximately 120 million tons of steel slag. Among this, basic oxygen furnace slag (BOFS) accounts for about 70 % of the total, exceeding 80 million tons [1–5]. Current disposal methods for BOFS, including landfilling and stockpiling, lead to resource wastage and environmental risks [6–8]. Previous studies have revealed that the oxide composition of BOFS shares significant similarities with that of cement clinker, indicating its potential use as an alternative cementitious binder [9–11]. However, BOFS contains a significant amount of inert iron oxides and low-reactivity minerals. During its cooling process, low-reactivity crystalline phases form, as a result, the application of BOFS as cementitious material is constrained [12–14].

Alkali-activated materials (AAM) represent a kind of low-carbon cementitious material produced from silicate precursor and alkali activators [15–17]. Since the precursors for the production of AAM are mainly industrial by-product, and do not necessitate high-temperature calcination [18], it generates significantly lower carbon dioxide emissions compared to cement production [19,20]. Additionally, compared to cement, AAM exhibit denser microstructure, higher early strength and superior resistance to acid, alkali and high temperature [21,22], thereby demonstrating great potential for large-scale applications in engineering [23,24].

AAM are typically categorized into two types according to their synthesis method: two-part AAM and one-part AAM [25–27]. In two-part AAM systems, a liquid alkali activator is first obtained by

* Corresponding author at: School of Civil Engineering and Architecture, Wuhan University of Technology, Luoshi Road 122, Wuhan 430070, China.
E-mail address: xushi@whut.edu.cn (S. Xu).

https://doi.org/10.1016/j.conbuildmat.2025.142514
Received 9 January 2025; Received in revised form 16 June 2025; Accepted 29 June 2025
Available online 4 July 2025

dissolving alkali salts in water, and this solution is subsequently mixed with precursors [28,29]. The high pH of the liquid alkali activator facilitates the dissolution and dissociation of precursors, thereby initiating hydration and hardening [30]. Nevertheless, the use of liquid alkali activator poses challenges for practical applications of AAM [31]. Firstly, liquid alkali activator requires precise control over the mix proportions and reaction conditions, complicating the application process [32]. Secondly, the storage and transportation of liquid alkali activator require specialized containers and conditions, further adding to transportation and management costs [33].

One-part AAM, also called "just-add-water" AAM, offers an innovative solution type by incorporating solid alkali activators directly with precursors [25,34]. This solid form eliminates the need for complex activator handling, reducing storage costs and minimizing environmental and safety risks [35,36]. Moreover, one-part AAM offers increased construction efficiency, making it suitable for on-site applications [37,38]. For example, Ma et al. [39] utilized three different sodium silicate (Na_2SiO_3) forms as solid activators with ground granulated blast furnace slag (GGBFS) precursor to prepare one-part AAM. They found that anhydrous Na_2SiO_3 exhibited the best activation effect compared with $Na_2SiO_3{\cdot}5\,H_2O$ and $Na_2SiO_3{\cdot}9\,H_2O$. When the anhydrous Na_2SiO_3 content was 10 wt%, one-part AAM's compressive strength achieved 76.3 MPa at 28 days. Yang, J. et al. [40] employed wet-ground fly ash (FA) and calcium carbide slag (CS) as precursors, and solid sodium metasilicate as activators to prepare one-part AAM. The results revealed that with 18 wt% CS content and 1 wt% sodium metasilicate content, one-part AAM's compressive strength achieved 32.1 MPa at 28 days. Ma et al. [41] used FA and GGBFS as precursors, sodium hydroxide (NaOH) and Na_2SiO_3 as solid alkali activators to synthesis one-part AAM. They found that when FA:GGBFS was 1:1, the 28d compressive strength of one-part AAM was the highest, reaching 28.3 MPa. The performance of one-part AAM is not inferior to that of two-part AAM, and its activation effect is similar to that of two-part system, which can effectively promote the dissolution and reaction of precursors [42]. Therefore, one-part AAM is comparable to two-part AAM in many performance indicators. In addition, one-part AAM has certain practical application advantages because it simplifies the treatment process of activators.

In recent years, many studies have explored using alkali fusion activation to improve the performance of one-part AAM [42,43]. This process involved mixing precursors with solid alkali activators and subjecting the mixture to calcination to enhance the reactivity of precursors. In comparison to the direct mixing of precursors with solid alkali activators, one-part AAM prepared via alkali fusion activation exhibited higher early strength and improved mechanical properties. Luo et al. [38] utilized alkali-fused lithium slag (LS) to prepare one-part AAM and examined how alkali fusion activation affects LS's reactivity and its subsequent effect on the mechanical performance of one-part AAM. They found that alkali fusion activation facilitated the dissolution of silicon and aluminium components in LS, improving its reactivity. The one-part AAM produced from alkali-fused LS achieved a compressive strength of 50.6 MPa at 28 days. Ye et al. [32] used red mud (RM) as precursors and prepared one-part AAM by alkali fusion activation. They found that when alkali-fused RM was dissolved, the soluble aluminosilicate released and created an alkaline environment, which helps to increase the Si/Al ratio of gel product, resulting in a more stable gel-network structure and higher compressive strength. Yang et al. [35] used alkali-fused molybdenum tailings (ML) and GGBFS to prepare one-part AAM and investigated its hydration mechanisms and microstructure. They found that the amorphous sodium aluminum silicate from the alkali-fused ML facilitated the hydration reaction between ML and GGBFS, generating C-(N-)A-S-H gels and leading to higher strength.

Many studies have investigated the synthesis of one-part AAM using alkali-fused solid waste as precursors. However, most previous research focuses on aluminosilicate-based precursors such as FA, GGBFS and RM [41,44,45], while there has been limited attention given to using alkali-fused basic oxygen furnace slag (ABOFS) as precursors to synthesis one-part AAM. BOFS inherently exhibits low reactivity, which hinders its use in alkali-activated materials. Although alkali fusion activation has been proved to be an effective method to improve the reactivity of precursors, it is still uncertain whether this method can sufficiently activate BOFS to make it a viable precursor for synthesizing one-part AAM. Several key issues remain unresolved. These include the lack of optimized parameters for the alkali fusion activation of BOFS, and the insufficient understanding of ABOFS's impact on the performance of one-part AAM. Furthermore, the environmental impact of one-part AAM with varying ABOFS contents, has not been assessed. Additional study is required to comprehend the potential of ABOFS in the synthesis of one-part AAM, and to provide new solutions for expanding the application of BOFS in sustainable alkali-activated materials.

This study aims to prepare ABOFS and to synthesize one-part AAM using ABOFS as precursors. Firstly, ABOFS was prepared with different contents of NaOH. The mineral phase, chemical functional groups and microstructure of ABOFS were studied. After optimizing the parameters for the preparation of ABOFS, one-part AAM was synthesized using ABOFS, GGBFS and anhydrous Na_2SiO_3 pellet. The compressive strength, mineral phase, chemical functional groups, reaction product, leaching characteristics, microstructure and pore structure of one-part AAM were tested. Finally, the environmental impact of one-part AAM prepared with different ABOFS content was evaluated. The main contribution of this study is the successful synthesis of one-part AAM using ABOFS as precursors. This study not only determined the optimal parameters for the preparation of ABOFS, but also proved the feasibility of using ABOFS to synthesis one-part AAM through the comprehensive evaluation of its performance. These findings provide a promising approach for the sustainable recycling of BOFS and demonstrate its potential as a low-carbon alternative for construction materials.

2. Materials and methods

2.1. Raw materials

In this study, BOFS and GGBFS were selected as the primary precursors. After alkali fusion activation of BOFS, GGBFS was used to supplement the silicon-aluminum component in precursors and further improve precursors' reactivity. BOFS and GGBFS were supplied by China Baowu Iron and Steel Group Co., Ltd. Commercially available industrial-grade NaOH and anhydrous Na_2SiO_3 with 99 % purity were used as solid alkali activators. X-ray fluorescence (XRF), laser particle size analysis and X-ray diffraction (XRD) tests were conducted to characterize the oxide composition, mineral phase composition and particle size distribution of BOFS and GGBFS. As presented in Table 1 and Fig. 1, respectively. The XRF test was performed using the pellet method. BOFS was pre-oxidized before the XRF test to ensure the conversion of FeO to Fe_2O_3. The total iron content in the BOFS was measured as Fe_2O_3, and the Loss on Ignition (LOI) values reported in Table 1 were determined prior to the oxidation process. Table 1 indicates that the main oxide composition of BOFS includes 45.38 % CaO, 11.81 % SiO_2 and 3.93 % Al_2O_3. As BOFS is the by-product of steelmaking, its Fe_2O_3 content is relatively high, reaching 26.11 %. The main oxide composition of GGBFS consists of 40.41 % CaO, 32.21 % SiO_2 and 17.28 % Al_2O_3. As shown in Fig. 1(b), the D_{50} and D_{90} particle sizes of BOFS are 19.8 μm and 68.5 μm, respectively, while for GGBFS, the corresponding particle sizes are 11.9 μm and 33.0 μm. XRD analysis reveals that the primary mineral phases in BOFS are Ca_2SiO_4 (C_2S), Ca_3SiO_5 (C_3S), portlandite, $Ca_4Al_2Fe_2O_{10}$ (C_4AF), hematite, calcite, $Ca_3Al_2O_6$ (C_3A) and RO phase. RO phase is the metal oxides solid solution formed as slag cools and solidifies during the steelmaking process, its main components are FeO, MnO and MgO. Due to the rapid cooling process during GGBFS formation, its structure is largely glass phase, as indicated by the broad hump distribution between $2\theta = 20^\circ$ and $2\theta = 40^\circ$ in Fig. 1(b).

Table 1
The oxide composition of BOFS and GGBFS.

Raw materials	SiO_2	Al_2O_3	CaO	Fe_2O_3	MgO	Na_2O	K_2O	P_2O_5	MnO	LOI
BOFS	11.82	3.93	45.38	26.11	3.82	0.16	0.11	1.93	2.92	3.82
GGBFS	32.21	17.28	40.41	0.51	7.42	0.37	0.45	0.02	0.15	1.18

LOI: loss of ignition.

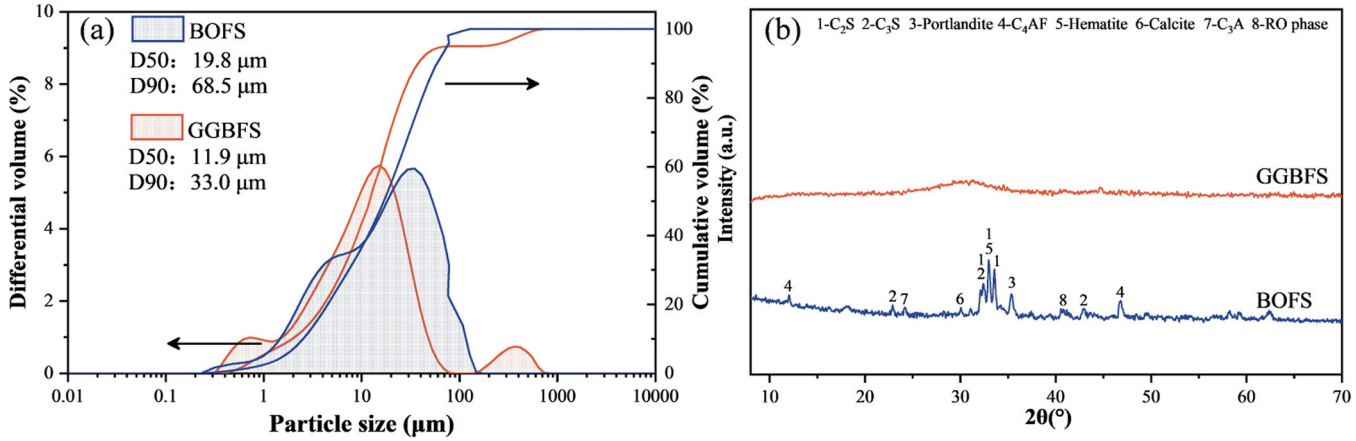

Fig. 1. (a) Particle size distribution and (b) mineral phase composition of BOFS and GGBFS.

2.2. Research program

The research program of this study is presented in Fig. 2. Firstly, BOFS was activated by alkali fusion with varying NaOH contents and characterized to examine the mineral phase, chemical functional groups and microstructure of ABOFS. Following the above test results, the optimum NaOH content was selected to prepare ABOFS, and then it was combined with GGBFS and anhydrous Na_2SiO_3 pellet to synthesis one-part AAM. The mechanical strength and leaching behaviour of one-part AAM pastes were tested. Moreover, XRD, Fourier-transform infrared spectroscopy (FTIR), thermogravimetric analysis (TGA), scanning electron microscope (SEM), energy dispersive spectroscopy (EDS) and mercury intrusion porosimetry (MIP) tests were conducted to characterize the microstructure and reaction products of one-part AAM. Finally, life cycle assessment (LCA) was performed on one-part AAM to quantify its environmental impact.

2.3. Preparation of ABOFS

TGA was conducted on BOFS to determine the optimal calcination temperature for alkali fusion activation. As shown in Fig. 3, the TG curve showed the thermal decomposition peaks near 400 °C and 600 °C. These two thermal decomposition peaks are associated with the existence of portlandite and calcite. When the temperature exceeded 800 °C, the weight of BOFS tended to be stable. This indicates that 800 °C is sufficient to induce mineral phase transformation in BOFS, which is beneficial for the subsequent alkali activation reaction. Considering the energy waste and unnecessary material decomposition associated with higher temperatures, 800 °C was determined to be the optimal temperature for alkali fusion activation. The alkali fusion activation parameters of BOFS are presented in Table 2. The NaOH content was set to 5 wt%, 10 wt% and 15 wt% (percentage by weight of BOFS). For each group of ABOFS, the calcination time was set to 60 min. During alkali fusion activation, NaOH was first thoroughly mixed with BOFS, and then the mixture was placed in the corundum crucible with 300 ML capacity and transferred to muffle furnace. The heating rate of the muffle furnace is set to 10 °C/min, once the temperature rose to 800 °C, it was maintained for 60 min. The mixture was then left to cool naturally to room temperature in the muffle furnace before being removed for further testing.

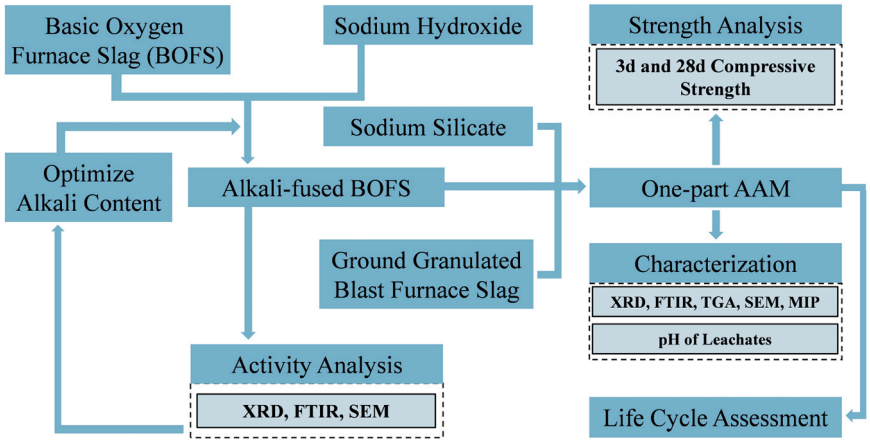

Fig. 2. The research program of this study.

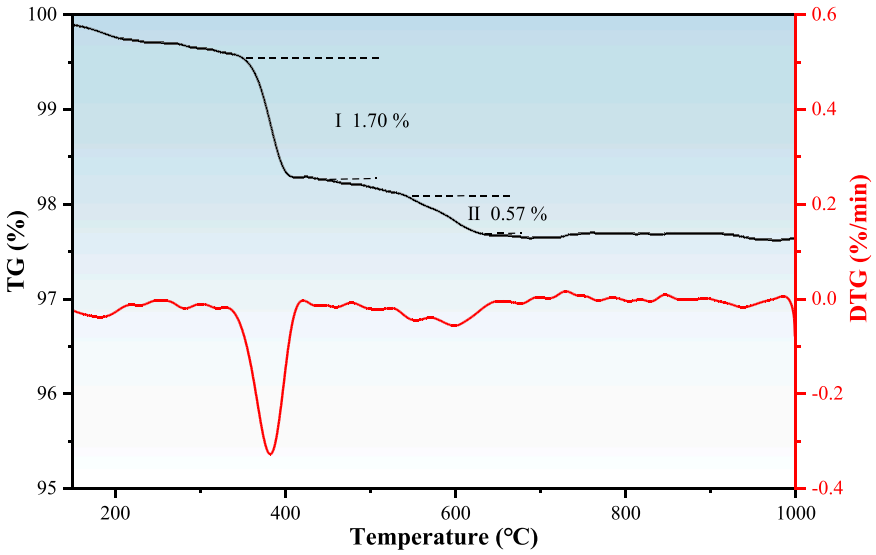

Fig. 3. TG and DTG curve of BOFS.

Table 2
The alkali fusion activation parameters of BOFS.

Sample ID	NaOH (wt %)	Calcination temperature/ °C	Thermostatic time/ min
BOFS-NH0	0	800	60
BOFS-NH5	5		
BOFS-NH10	10		
BOFS-NH15	15		

2.4. Preparation of one-part AAM

Table 3 shows the mix proportions of all groups of paste. Firstly, the optimum NaOH content was selected according to the characterization results of ABOFS. The ABOFS prepared with the optimal NaOH content was then combined with GGBFS and anhydrous Na_2SiO_3 pellet, ground in a planetary ball mill (Chishun QM-3SP04, China) at 200 rpm for 5 min to prepare uniform powdered mixture, as depicted in Fig. 4. The mixture was then mixed with water and stirred for 2 min to obtain one-part AAM paste. To provide a more direct comparison of the reactivity between BOFS and ABOFS, control groups paste was prepared by replacing ABOFS with an equivalent weight of BOFS and following the same procedure. All paste was transferred into 40 × 40 × 40 mm molds, vibrated for 1 min, and then sealed using plastic film. After 24 h, the pastes were removed from the molds and then cured further in the curing chamber (20 ± 2°C, 95 ± 2 % RH) for 2, 6, and 27 days for subsequent testing.

Table 3
Mix proportion of one-part AAM paste and control groups paste.

Sample ID	ABOFS/g	BOFS/g	GGBFS/g	Na_2SiO_3/g	Water/g
OAAM−1	400	0	0	60	230
OAAM−2	320		80		
OAAM−3	240		160		
OAAM−4	160		240		
OAAM−5	80		320		
CG−1	0	400	0		
CG−2		320	80		
CG−3		240	160		
CG−4		160	240		
CG−5		80	320		

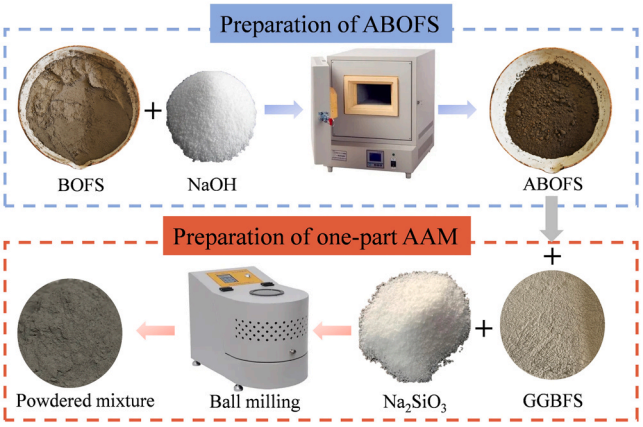

Fig. 4. Preparation of one-part AAM.

2.5. Experimental method

2.5.1. Microscopic test

Since ABOFS will agglomerate after calcination, it was ground into the powder with a particle size of less than 0.075 mm before microscopic tests. XRD and FTIR tests were carried out on BOFS and ABOFS to investigate how the activation affected its mineral composition and chemical functional groups. XRD, FTIR and TGA were performed on one-part AAM pastes cured for 28d to analyze its phase assemblage, chemical functional groups and reaction products. Before testing, the one-part AAM paste was crushed, and the central part of the paste samples was immersed in anhydrous ethanol for 7 days to inhibit hydration. Afterward, the samples were vacuum-dried at 40 °C for 24 h to eliminate any remaining ethanol. Finally, the dried samples were ground into powders with a particle size smaller than 0.075 mm. The X-ray diffractometer (Tongda TD-3500, China) was set with the scanning range of 10 ° to 70 ° and the scan speed of 1 °/min. A copper X-ray tube was used for the measurements. The scan was performed with a step size of 0.02 ° (2θ). For qualitative phase identification, the HighScore Plus software was employed, utilizing the International Centre for Diffraction Data (ICDD) database for phase matching. The infrared spectrometer (Delite DH108, China) was set to a detection range of 400–4000 cm^{-1}. For TGA, the thermogravimetric analyzer (Netzsch TMA402F3, Germany) was set to a heating rate of 10 °C/min, from 30 °C to 1000 °C. SEM and EDS test

(Zeiss Gemini 300, Germany) was conducted to observe the microstructure and determine the elemental composition of ABOFS and one-part AAM. Before the test, the platinum coating was applied to the surface of the paste sample to improve its conductivity. Electron Probe Microanalyzer (JEOL JXA-8230, Japan) was used to perform back-scattered electron (BSE) imaging on the paste samples to analyze their Ca/Si, Na/Si, Mg/Si and Al/Si ratios. Before the test, the central portion of the paste samples was sealed with epoxy resin, then polished sequentially using sandpapers of 200, 400, 800, 1200, 2000, and 4000 mesh, followed by polishing with 3 μm polishing fluid. To enhance the conductivity of the samples, a carbon conductive layer is sprayed on the samples. The pore structures of paste samples were characterized by MIP (Auto Pore 9500, USA).

2.5.2. Leaching test

The leaching characteristics of one-part AAM pastes in alkaline solution was investigated by measuring the pH of the leachates. Reaction-stopped one-part AAM pastes powder with a particle size of less than 0.075 mm was leached in deionized water for 24 h based on the liquid-solid ratio of 50:1, the supernatant was separated, and the leachate's pH was measured.

2.5.3. Compressive strength test

The 3d and 28d compressive strength of paste were measured by the electronic universal testing machine (Yixuan TYE-3000, China). The loading speed of the pressure is set to 2.4 kN/s. Each group of pastes was tested 6 times. The results including average compressive strength and standard deviation were reported.

2.6. Life cycle assessment

In accordance with international standard ISO 14040 [46], the cradle-to-gate LCA of ordinary Portland cement (OPC) and one-part AAM with varying GGBFS contents (0 wt%, 20 wt%, 40 wt%, 60 wt%, and 80 wt%) was conducted using SimaPro (version 9.0.0.48) software. The functional unit was established as 1 kg of OPC and one-part AAM. Fig. 5 illustrates the system boundaries of this study, which include the production and acquisition of raw materials, transportation of raw materials to the cement plant (Assuming production is completed here), and the processing of raw materials and one-part AAM production. The following assumptions were taken into account for the current LCA: 1) BOFS and GGBFS are regarded as metallurgical solid waste, and the analysis considers only the emissions associated with their downstream processing and transportation. 2) Results of TGA indicate that the CO_2 emission during the calcination of BOFS at 800 °C is less than 1 % of the weight of the BOFS; therefore, the CO_2 emission from ABOFS can be neglected. 3) The energy consumption for each unit operation/process was calculated using rated power, operating time and output. In the absence of specific data, power parameters from common production equipment in the Chinese market were used, without considering the manufacturing and maintenance of the production equipment. 4) The usage and disposal phases of one-part AAM and OPC are excluded from this study, as they are expected to produce similar environmental impacts during these stages.

Table 4 presents the life cycle inventory (LCI) analysis for one-part AAM, quantifying the material and energy input values for the three stages of producing 1 kg one-part AAM. Given that BOFS and GGBFS were by-products of the steel industry, the transportation distance for BOFS and GGBFS from the steel plant to the cement plant was set at 100 km (a relatively long distance), while the distance for transporting NaOH and Na_2SiO_3 from the market to the cement plant was set at 50 km. To achieve a more accurate calculation of the energy input values for producing 1 kg one-part AAM, commonly used production equipment in the Chinese market was considered. Specifically, the power of the jaw crusher was 37 kWh, the processing capacity was 35t/h. The power of the ball mill was 250 kWh, the processing capacity was 10t/h. The power of the industrial muffle furnace was 100 kWh, with a heating rate of 10 °C/min, capable of calcining 3 tons of ABOFS in each batch. The Ecoinvent database was utilized to gather data related to the production processes of OPC and one-part AAM, while the environmental impacts of both OPC and one-part AAM were evaluated using SimaPro software. The overall environmental impact of the prepared mixtures was evaluated using the "Tool for the Reduction and Assessment of Chemical and Other Environmental Impacts" (TRACI) method, focusing on four environmental impact indicators: global warming potential (GWP), ozone depletion potential (ODP), acidification potential (AP), and energy consumption (EC).

3. Results and discussion

3.1. Characterization of ABOFS

3.1.1. XRD and FTIR analysis

The XRD patterns of BOFS and ABOFS are shown in Fig. 6(a). After calcination at 800 °C, the diffraction peaks of portlandite and calcite in the XRD pattern of BOFS-NH0 disappeared, and two new phases were observed, which were the CaO diffraction peak at 37.5 ° and the wuestite diffraction peak at 42 °. The formation of CaO is attributed to the thermal decomposition of portlandite and calcite, while the presence of wuestite may result from the incomplete oxidation of zero-valent iron in

Table 4
Inventory data for 1 kg one-part AAM production.

Description	OAAM-1	OAAM-2	OAAM-3	OAAM-4	OAAM-5
Raw material input in (kg)					
BOFS	0.79	0.63	0.47	0.32	0.16
NaOH	0.08	0.06	0.05	0.03	0.02
GGBFS	0.00	0.17	0.35	0.52	0.70
Na_2SiO_3	0.13	0.13	0.13	0.13	0.13
Transportation (kgkm)					
BOFS	79.10	63.20	47.40	31.60	15.80
NaOH	3.90	3.15	2.35	1.60	0.80
GGBFS	0.00	17.40	34.80	52.20	69.60
Na_2SiO_3	6.50	6.50	6.50	6.50	6.50
Production					
Energy (MJ)	0.41	0.34	0.28	0.22	0.15

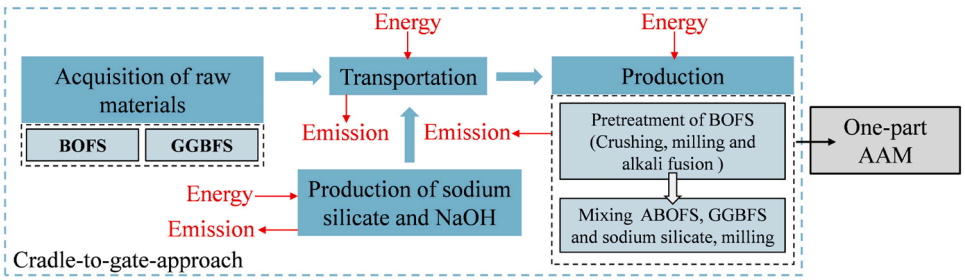

Fig. 5. System boundaries for one-part AAM production.

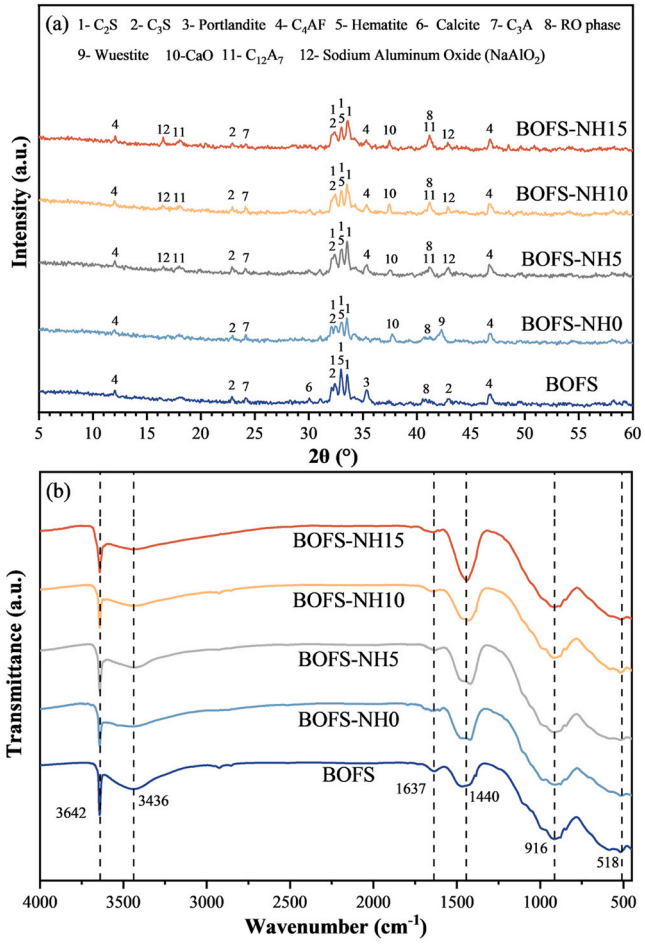

Fig. 6. XRD and FTIR curves of BOFS and ABOFS, (a) XRD patterns, (b) FTIR curves.

BOFS during high-temperature calcination. After alkali fusion activation, the diffraction peaks of $Ca_{12}Al_{14}O_{33}$ ($C_{12}A_7$) and $NaAlO_2$ appeared in the XRD pattern of BOFS-NH5. The formation of $C_{12}A_7$ is attributed to a solid-state reaction between CaO and Al_2O_3, while $NaAlO_2$ is produced from the reaction between C_3A and NaOH. Notably, a new diffraction peak of C_4AF emerged around 35°, which is likely due to the reaction of CaO with C_3A and wuestite, leading to the formation of additional C_4AF. This also explains why the diffraction peak of wuestite in the XRD pattern of BOFS-NH5 disappears. In addition, the C_2S diffraction peak's intensity increases as NaOH content increases, this may be because the high content of iron oxide in BOFS has fluxing effect, which will promote the development of calcium silicate phase [47]. Moreover, during fusion activation, the crystalline phase in BOFS will react with OH^- at high temperature to form reaction phases such as C_2S [48]. In summary, alkali fusion activation promoted the formation of reactive mineral phases such as C_2S, C_4AF, $C_{12}A_7$ and $NaAlO_2$ in BOFS, which contributes to enhancing the hydration activity of BOFS.

The FTIR spectra of BOFS and ABOFS are presented in Fig. 6(b). The vibration band at 3642 cm^{-1} corresponds the stretching vibration of -OH, indicating the presence of portlandite. The portlandite in BOFS is not completely decomposed at 800 °C, so the absorption peak of -OH still exists in the FTIR spectra of ABOFS, but its intensity is weaker than that of BOFS. The vibration bands at 3436 cm^{-1} and 1637 cm^{-1} correspond to the stretching and bending vibrations of -OH, respectively. These characteristic absorption peaks are attributed to the bound and free water present in BOFS. However, there is no free water inside ABOFS after high-temperature calcination. This indicates that under high-temperature conditions, BOFS may react with NaOH, resulting in the formation of products that contain chemically bound water. The vibration band at 1440 cm^{-1} corresponds to the asymmetric stretching vibration of CO_3^{2-}. This may be because the excessive NaOH will react with CO_2 to form microcrystalline Na_2CO_3. The vibration band at 916 cm^{-1} corresponds to the stretching vibration of Si-O in C_2S, while the vibration band at 518 cm^{-1} is associated with the stretching vibration of Fe–O in hematite.

3.1.2. Micromorphology of BOFS and ABOFS

The micromorphology of BOFS and ABOFS are displayed in Fig. 7. BOFS particles exhibit a smooth surface with clear edges. The small particles on its surface may be related to the residual secondary minerals or impurity particles during its formation. However, the micromorphology of BOFS-NH10 changed significantly, its particle surfaces become looser, and full of disordered flocculent products. This transformation indicates that alkali fusion activation affects the physical properties of BOFS particles, the original surface structure of BOFS was partially destroyed, resulting in a significant increase in specific surface area. Therefore, alkali fusion activation can increase the contact area between the internal mineral phase of ABOFS and the alkaline solution. It is evident that when the NaOH content is 5 wt%, the alkali fusion activation has a limited effect on modifying BOFS particles due to the insufficient alkali content. When the NaOH content is 15 wt%, although the ABOFS particles exhibit a rougher surface, the increased raw material costs associated with the higher NaOH content reduce the economic feasibility of ABOFS. Therefore, considering the micromorphology, mineral phase composition and economic feasibility of ABOFS, the optimal NaOH content is determined to be 10 wt%.

3.2. Characterization of one-part AAM

According to the characterization results of ABOFS, the optimum NaOH content for alkali fusion activation is 10 wt%. Therefore, BOFS-NH10 was selected to prepare one-part AAM pastes for subsequent characterization.

3.2.1. Leaching characteristics of one-part AAM pastes

The pH of the leachates of one-part AAM pastes after curing for 3d, 7d and 28d are shown in Fig. 8. As reported by Song et al. [49], the Si and Al components in GGBFS only dissolve significantly and participate in reaction when the pH is above 11.5 in the system. It is clear that the leachates of one-part AAM pastes remain alkaline, with pH ranging from 11.94 to 12.56. This indicates that ABOFS provides an important alkaline environment for pastes, and offers a suitable chemical environment for prolonged reactions, so that the reaction is not limited to the early stage, but also can continue to generate reaction products in the later stage.

For the same curing duration, the pH of the leachates decreases as GGBFS content increases. This is because the decrease of ABOFS content reduces the free alkali content in pastes. Additionally, due to the greater reactivity of GGBFS, the higher GGBFS content will lead to an increased consumption of alkali during the reaction. For each group of one-part AAM pastes, the pH of the leachate decreases with curing time. This is because the Si and Al components in precursors continuously dissolve, consuming the free alkali in the system. It is noteworthy that the leachates' pH decreased faster when curing 3d to 7d, and then slowed down when curing 7d to 28d. This is because the decreasing alkalinity in later stage of curing reduces the reaction rate, further slowing down the pH decrease.

3.2.2. XRD test

The XRD patterns of one-part AAM pastes cured for 28d are presented in Fig. 9. It is clear that compared to BOFS-NH10, new phases were generated in OAAM-1, including katoite, C-S-H gel, C-(N-)A-S-H gel and hydrotalcite. Additionally, unreacted C_2S still exists in OAAM-1. This is due to the relatively low content of active Ca, Si, and Al in OAAM-

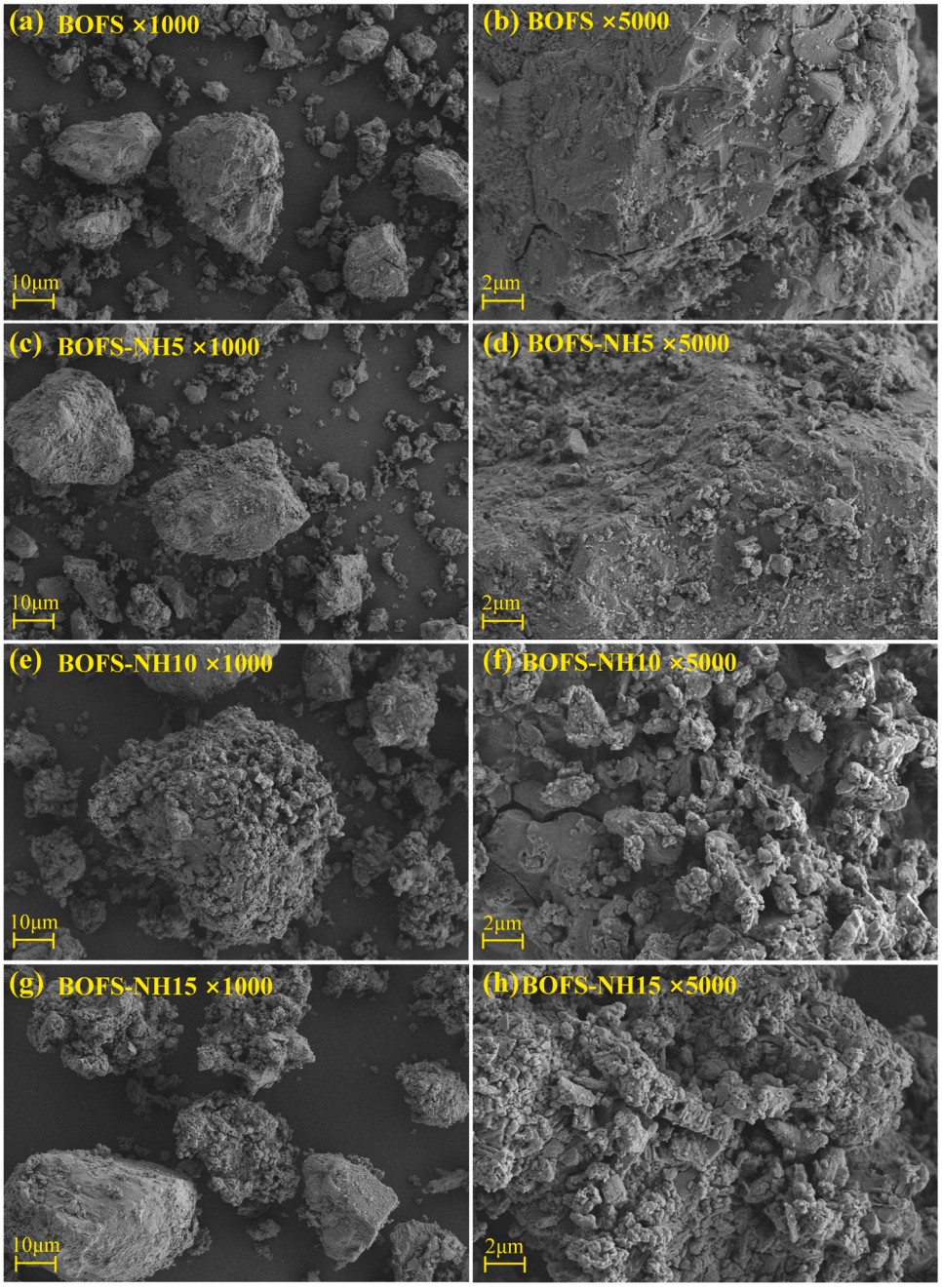

Fig. 7. Micromorphology of BOFS and ABOFS, (a) and (b) BOFS, (c) and (d) BOFS-NH5, (e) and (f) BOFS-NH10, (g) and (h) BOFS-NH15.

1, resulting in the ABOFS are not completely reacted. With the addition of GGBFS with higher reactivity, the amorphous gel phase began to appear in XRD patterns, which corresponded to the hump-shaped diffraction peak between 25°-35° in XRD patterns. As reported by Liu et al. [50], this diffraction peak represents the presence of amorphous C-(N-)A-S-H gel. According to the XRF results, the content of MgO in GGBFS is 7.4 wt%. Under alkaline conditions, Mg^{2+} is dissolved from GGBFS and reacted with aluminum components to form hydrotalcite. Therefore, with the increase of GGBFS, the additional hydrotalcite phase appear at 11.5 °. It is noteworthy that as the GGBFS content rose, the intensity of gel's characteristic peaks first increased and then decreased. This is because the reactivity of GGBFS is higher, so the crystalized reaction products will increase with the increase of GGBFS. However, when the content of GGBFS reached 80 wt%, although the content of reactive components in the system is high, the significantly reduced alkalinity due to the low ABOFS content leads to a decrease in the amount of reaction products, which will be further supported by the results of TGA.

3.2.3. *FTIR test*

The FTIR curves of one-part AAM pastes cured for 28d are presented in Fig. 10. The vibration band at 1659 cm^{-1} is attributed to the bending vibration of the O-H bonds. This characteristic peak points to the existence of chemically bound water, confirming the formation of hydrated products. The vibration bands at 1454 cm^{-1}, 1411 cm^{-1} and 866 cm^{-1} are attributed to the bending vibration and stretching vibration of the C-O bonds, suggesting the presence of carbonate products in one-part AAM pastes. This is attributed to the exposure of one-part AAM pastes to CO_2 in the air during curing, resulting in carbonation. It is evident that these three characteristic peaks in the spectra of OAAM-1 are sharper, whereas

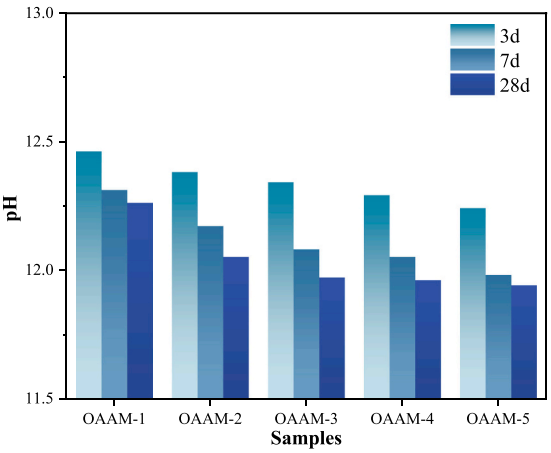

Fig. 8. The pH of the leachates of one-part AAM pastes after curing for 3d, 7d and 28d.

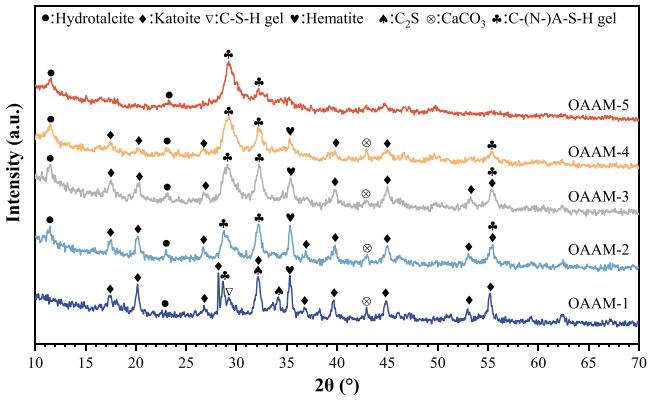

Fig. 9. XRD patterns of one-part AAM pastes cured for 28d.

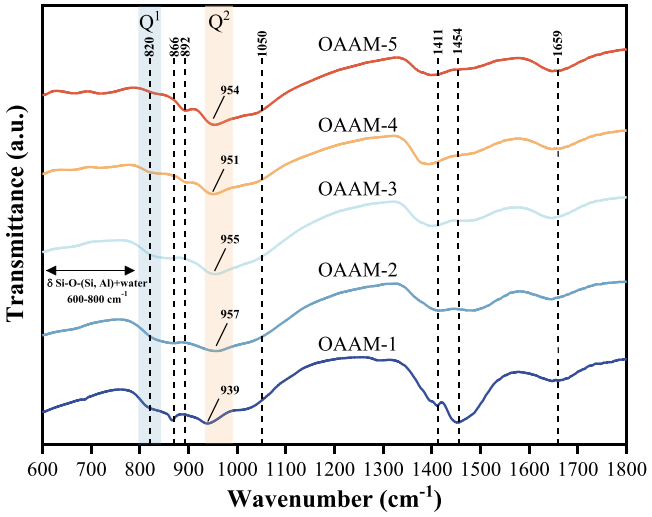

Fig. 10. FTIR spectra of one-part AAM pastes cured for 28d.

these peaks are significantly weakened after the addition of GGBFS. According to the Ref [51,52], sharper peaks indicate the higher degree of crystallization, while higher wavenumber indicate the higher polymerization degree of the structure. Therefore, it can be inferred that the degree of carbonization of one-part AAM decreases with the addition of GGBFS, which aligns with the XRD results. The vibration band at 892 cm^{-1} is attributed to the bending vibration of Si-O bonds. It is worth noting that OAAM-4 and OAAM-5 showed more pronounced intensity in this wavenumber, which may be due to the increase in Ca content within the gels as the GGBFS content rises, leading to a more ordered gel structure [50]. The vibration bands in the range of 600–800 cm^{-1} correspond to bending vibrations of Si-O-Si(Al) groups and the vibration of water molecules [53]. The band at approximately 820 cm^{-1} corresponds to the Si–O stretching vibrations of the Q^1 unit [54]. The band at approximately 950 cm^{-1} corresponds to the asymmetric stretching vibration of Si-O-T (T = Si, Al) and/or Si-O-M (M = alkali metal elements) of the Q^2 unit [50]. The small shoulder near 1050 cm^{-1} is attributed to the asymmetrical stretching vibration of Si-O bonds [54]. These characteristic peaks verify the generation of C-S-H and C-(N-)A-S-H gel. Since GGBFS will introduce a significant quantity of soluble Si, the Ca/Si ratio of one-part AAM will decrease with the addition of GGBFS (see Section 3.2.5). As reported in Ref [55], the content of Q^1 unit decreases with the decrease of Ca/Si ratio. Therefore, the Q^1 unit intensity of one-part AAM decreases as the GGBFS content increases. In addition, compared with OAAM-1, the wavenumbers of Q^2 unit increased after the addition of GGBFS. This indicates that the C-(N-)A-S-H gel's polymerization degree rose with the addition of GGBFS [56].

3.2.4. TGA

The TGA results of one-part AAM pastes are displayed in Fig. 11. According to Refs [57–60], the reaction products in AAM can be identified based on weight loss observed across the specific temperature ranges: C-(N-)A-S-H gels (30–200 °C), hydrotalcite-like phases (200–400 °C) and calcium carbonate (600–900 °C). Furthermore, the bound water content, determined by the weight loss up to 650 °C, reflects the overall amount of reaction product formation, as illustrated in Fig. 12.

As illustrated in Fig. 12(a) and (d), when the GGBFS content does not exceed 60 wt%, both the gel content and the total bound water in one-part AAM pastes increase as the GGBFS content rises. This suggests that with the increase of GGBFS, more reaction products are produced in one-part AAM pastes. Nevertheless, when the GGBFS content reached 80 wt%, the gels and total bound water in OAAM-5 is lower than OAAM-4. This is because that as the GGBFS content increased to 60 wt%, due to the high reactivity of GGBFS, the amount of crystallization reaction products in the one-component AAM paste increased. However, when the GGBFS content reached 80 wt%, although the content of reactive components in pastes is high, the low ABOFS content significantly reduced the alkalinity of pastes, which decreased GGBFS's reaction degree and ultimately reduced the formation of reaction products. As shown in Fig. 12(b), after the addition of GGBFS, the hydrotalcite in OAAM-2 paste increased significantly compared with OAMM-1 paste. This is because the content of Mg and Al in GGBFS is higher, which promotes the formation of hydrotalcite. However, the hydrotalcite in

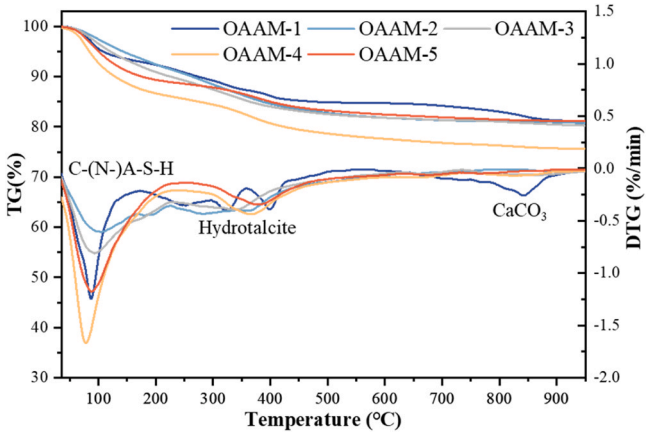

Fig. 11. TG and DTG of one-part AAM pastes cured for 28d.

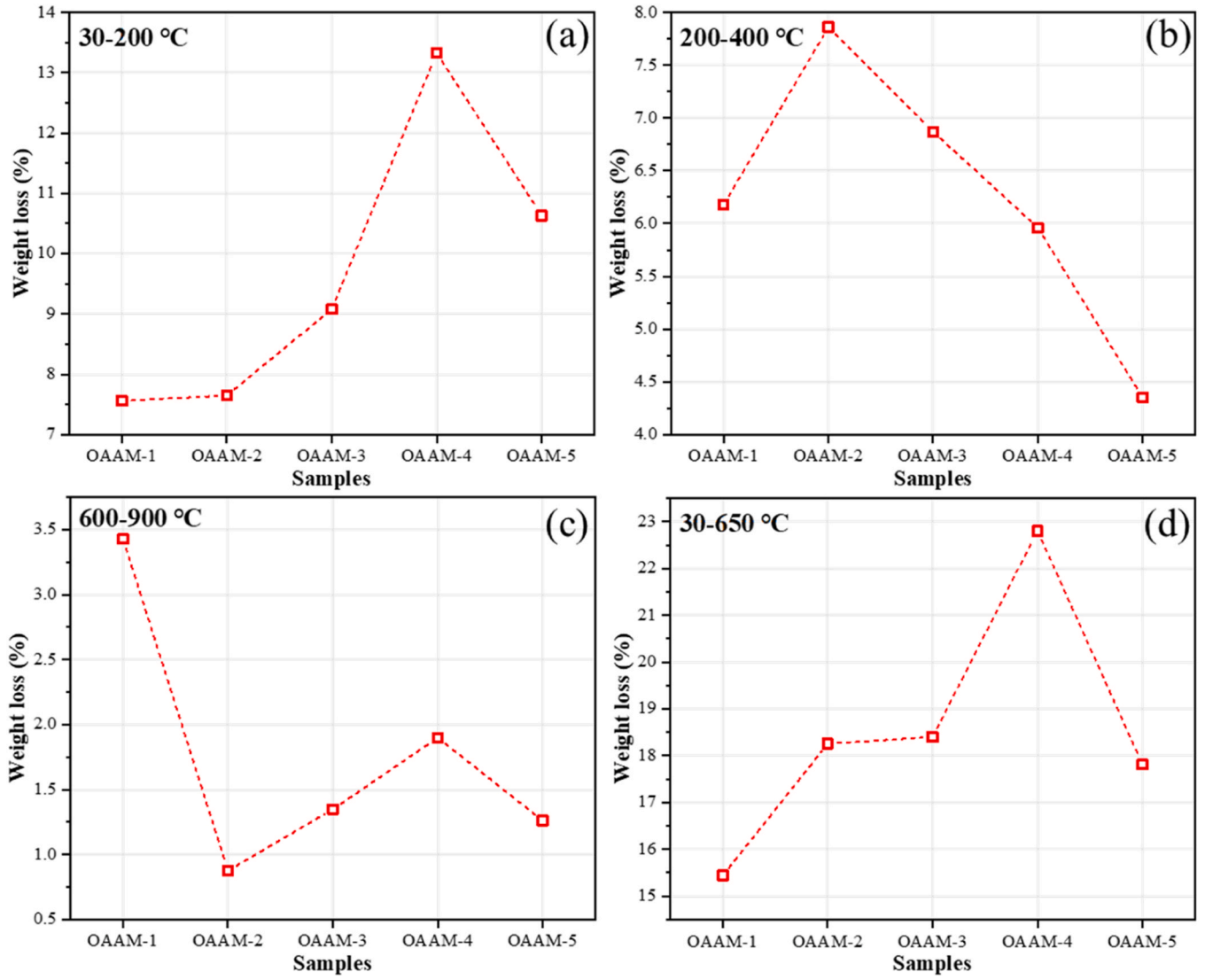

Fig. 12. Mass-normalized weight loss of one-part AAM pastes throughout a range of temperatures: (a) 30–200 °C, (b) 200–400 °C, (c) 600–900 °C and (d) 30–650 °C.

OAAM-3 paste and OAAM-4 paste decreased compared with OAAM-2 paste. This decrease in hydrotalcite may be due to stronger carbonation, this is in line with the findings in Fig. 12(c). When the GGBFS content increased to 80 wt%, although the calcium carbonate in OAAM-5 paste decreased compared with OAAM-4 paste, the hydrotalcite in OAAM-5 paste also decreased significantly compared with OAAM-4 paste. This may be because the decrease of alkalinity in paste inhibits the formation of hydrotalcite.

3.2.5. SEM analysis

The micromorphology and EDS spectrum of one-part AAM pastes are presented in Fig. 13. It can be seen that the micromorphology of different groups of one-part AAM pastes showed significant differences. As shown in Fig. 13(a), OAAM-1 showed a relatively loose structure due to the limited formation of gel products. Fig. 13(b) shows that the main elements of the reaction products in OAAM-1 are Ca, Na, O, and Si, with a relatively low Al content. It can be inferred that it is mainly composed of C-S-H gel and excessive unreacted alkali. From Fig. 13(c), it can be seen that the micromorphology of OAAM-3 is denser than that of OAAM-1, which is due to the incorporation of GGBFS to supplement the silicon and aluminum components in the system, thus promoting the hydration reaction. The reaction products will fill the pores and cracks in the sample and improve its compactness. Fig. 13(d) indicates that the main elements of the reaction products in OAAM-3 are Ca, O, Si, Na and Al, which can be inferred that it is mainly composed of C-(N-)A-S-H gel. It can be observed from Fig. 13(e) that OAAM-5 has the densest micromorphology. Fig. 13(f) shows that the Na/Si ratio of the reaction product in OAAM-5 is lower than that of OAAM-3. This indicates that with the decrease of ABOFS, the degree of Na incorporation into C-A-S-H gel in OAAM-5 decreased.

The BSE images of one-part AAM pastes are presented in Fig. 14. It can be seen that there are unreacted phases in OAAM-1 and OAAM-5, and their elemental composition is shown in Table 5. It can be determined that the unreacted phase in OAAM-1 is ABOFS particles, while the unreacted phases in OAAM-5 are GGBFS particles and ABOFS particles. The unreacted phases in OAAM-3 are less than that in OAAM-1 and OAAM-5.This may be because as mentioned in Section 3.2.3, GGBFS has relatively higher reactivity, when its content increases from 0 wt% to 40 wt%, GGBFS will promote the hydration reaction, resulting in the reduction of unreacted phases in OAAM-3. However, when the GGBFS content increased to 80 wt%, as the reaction proceeds, not only the alkalinity of pastes will decrease, but also the hydration products will accumulate around the unreacted GGBFS particles, hindering the ion exchange between the interior of GGBFS and alkali solution, thereby inhibiting the further reaction of GGBFS.

Fig. 15 presents the atomic Na/Si ratio and Ca/Si ratio of one-part

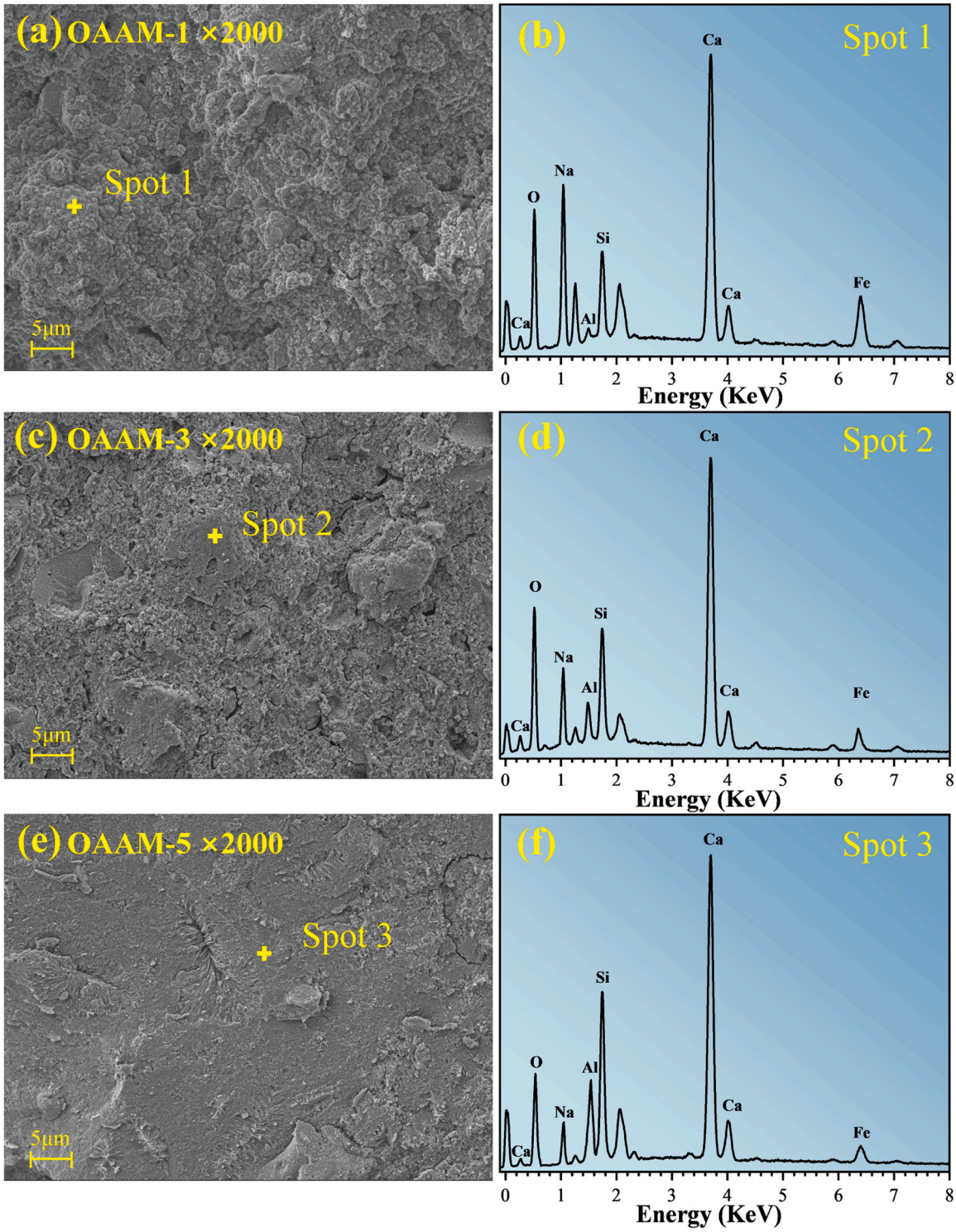

Fig. 13. Micromorphology and EDS spectrum of one-part AAM pastes: (a), (c) and (e) Micromorphology; (b), (d) and (f) EDS spectrum.

AAM pastes, with 50 points analyzed in each paste. Since the addition of GGBFS will introduce a significant quantity of soluble Si ions into pastes, the Ca/Si ratio of one-part AAM pastes decreases with the addition of GGBFS. However, when the GGBFS content remains constant, there is little variation in Ca/Si ratio between 7d and 28d. Notably, the Na/Si ratio of OAAM-1 and OAAM-5 increased significantly from 3d to 28d, while the Na/Si ratio of OAAM-3 decreased from 3d to 28d. In OAAM-1, the pore solution contains a high content of Na and Si ions, but the content of Ca ions is comparatively low due to the lack of GGBFS in the system. Therefore, during the hydration process, Na ions play a more important role in maintaining charge balance between the layers of C-(N-)A-S-H gels, resulting in the increase of Na/Si ratio of OAAM-1 with the hydration reaction. In OAAM-3, with the addition of GGBFS, the Na ions concentration in pore solution decreased, while the Si ions concentration increased. On the other hand, Ca ions were continuously dissolved from GGBFS, and Na was gradually replaced by Ca in C-(N-)A-S-H gels, so the Na/Si ratio of OAAM-3 decreased over curing time. In OAAM-5, the Na ions content in pore solution was further decreased.

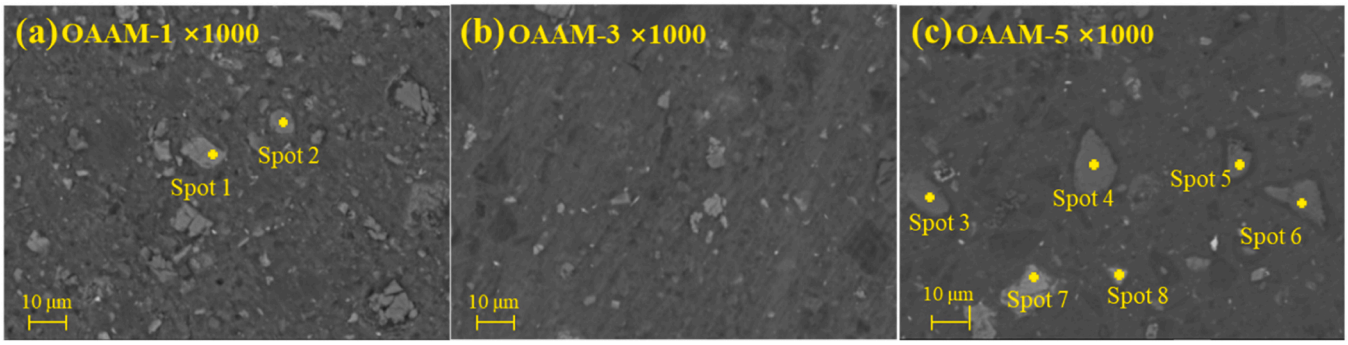

Fig. 14. BSE images of one-part AAM pastes: (a) OAAM-1, (b) OAAM-3 and (c) OAAM-5.

Table 5
Elemental composition of one-part AAM pastes (atom %).

	C	O	Ca	Si	Al	Na	Mg	Fe
Spot 1	15.96	27.68	17.02	6.28	1.04	3.82	2.37	25.83
Spot 2	12.46	36.53	18.58	3.85	0.73	3.96	3.69	20.20
Spot 3	13.71	56.10	13.13	8.50	2.20	1.99	3.32	1.05
Spot 4	12.76	56.55	13.53	8.41	4.03	1.12	3.14	0.46
Spot 5	7.94	55.23	16.36	8.23	5.64	1.54	4.37	0.69
Spot 6	5.66	59.17	12.57	11.84	6.08	0.59	3.45	0.64
Spot 7	9.02	51.11	17.12	1.06	2.00	4.38	2.04	13.27
Spot 8	11.04	52.03	9.58	6.97	1.19	4.88	3.78	10.53

However, as mentioned above, the unreacted GGBFS particles in OAAM-5 increased, so the content of Ca ions dissolved from GGBFS decreased. Over time, Ca could not completely replace Na in C-(N-)A-S-H gels, resulting in an increase in Na/Si ratio, but the increase is less pronounced than that observed in OAAM-1.

Fig. 16 presents the atomic Mg/Si and Al/Si ratios of one-part AAM pastes, along with their linear correlation. According to previous studies [61], the linear correlation between Mg/Si and Al/Si suggests the formation of hydrotalcite-like phase, while the positive X-axis intercept reflects the degree of Al incorporation into C-S-H gel. The Al/Si ratio of one-part AAM pastes rose as the GGBFS content increased. This is because the addition of GGBFS with high Al_2O_3 content will promote more Al incorporation into the C-S-H gel [54], as well as seen in the growth of the X-axis intercept on the Al/Si axis in Fig. 16. At 3 days of curing, the linear correlation between Mg/Si and Al/Si of OAAM-1 is weak, which may be due to the low content of Mg and Al in ABOFS, resulting in less hydrotalcite-like phase formed in pastes. The Mg/Al ratio of OAAM-3 and OAAM-5 increases with time, which may be due to the low Mg/Al ratio of unhydrated GGBFS. As curing time progressed, the unhydrated GGBFS in pastes gradually decreased, and the hydrotalcite phase gradually increased, leading to a rise in Mg/Al ratio. At 28 days of curing, the Mg/Al ratios of OAAM-1, OAAM-3 and OAAM-5 are in the range of 1.92–4.35, representing the hydrotalcite formed in one-part AAM pastes [62].

3.2.6. *Hydration mechanism of one-part AAM paste*

According to the results of the above tests, the hydration process of one-part AAM can be summarized as follows:

1. Anhydrous Na_2SiO_3 and the highly reactive mineral phases in ABOFS, such as $C_{12}A_7$, $NaAlO_2$ and C_3A, dissolve in water, releasing Ca^{2+}, Na^+, $[Al(OH)_4]^-$ and OH^-, which significantly increases the pH of the pore solution. This stage primarily occurs at the particle surface, providing the alkaline environment and essential ions for the subsequent hydration reactions.
2. Under the alkaline conditions, C_3S and C_2S in ABOFS, as well as the glass phase in GGBFS, continue to dissolve, releasing Ca^{2+}, $[SiO_4]^{4-}$ and $[Al(OH)_4]^-$. The primary hydration products at this stage consist of C-S-H gel, $Ca(OH)_2$ and katoite ($Ca_3Al_2(OH)_{12}$), as shown in the following equation [63]:

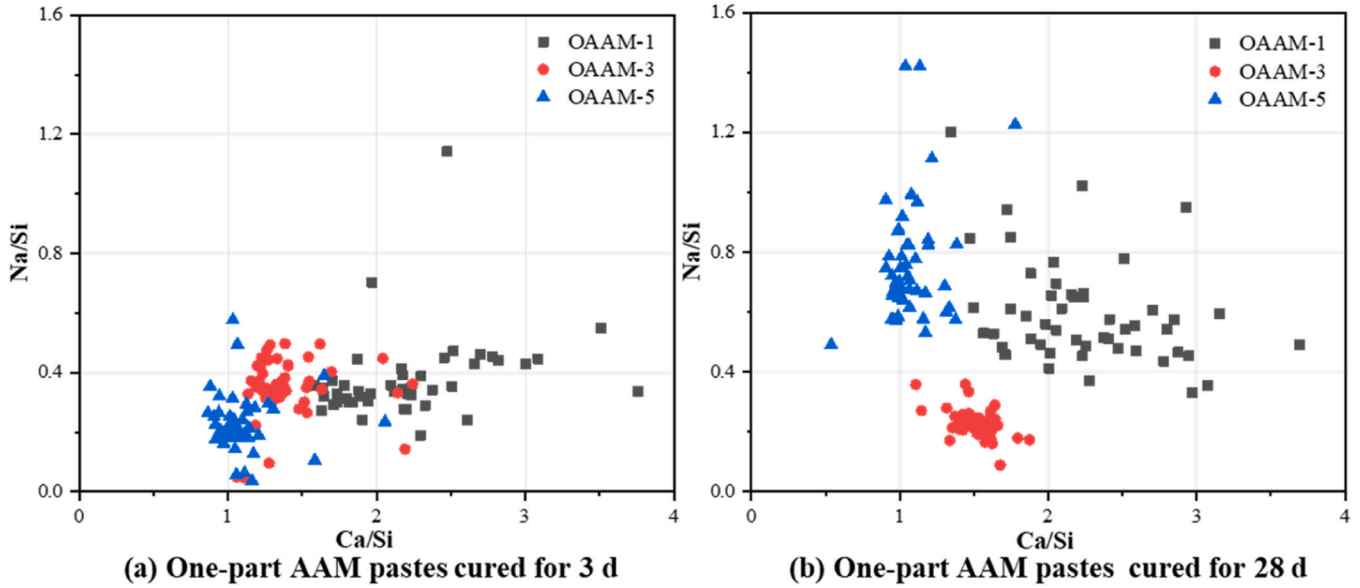

Fig. 15. Atomic Na/Si ratio versus Ca/Si ratio of one-part AAM pastes, (a) Cured for 3d, (b) Cured for 28d.

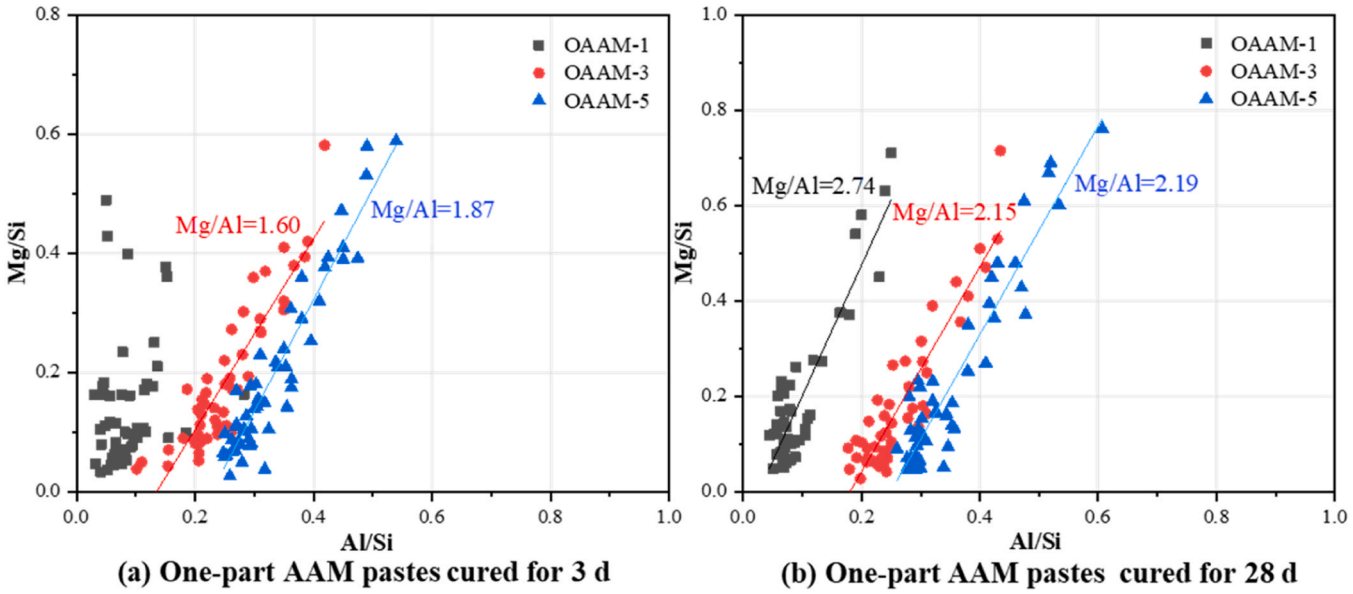

Fig. 16. Atomic Mg/Si ratio versus Al/Si ratio of one-part AAM pastes, (a) Cured for 3d, (b) Cured for 28d.

$$xCa^{2+} + [SiO_4]^{4-} + yH_2O \rightarrow xCaO{\cdot}SiO_2{\cdot}yH_2O \quad (1)$$

$$Ca^{2+} + 2OH^- \rightarrow Ca(OH)_2 \quad (2)$$

$$3Ca^{2+} + 2[Al(OH)_4]^- + 6H_2O \rightarrow Ca_3Al_2(OH)_{12} \quad (3)$$

3. As $Ca(OH)_2$ continues to form, the alkalinity of the system increases, which further promotes the dissolution of the glass phase in GGBFS, releasing large quantities of $[SiO_4]^{4-}$, $[H_3SiO_4]^-$ and $[H_3AlO_4]^{2-}$. $Ca(OH)_2$ reacts with $[SiO_4]^{4-}$ to form C-S-H gel, while Na^+ and Ca^{2+} in the system react with $[H_3SiO_4]^-$ and $[H_3AlO_4]^{2-}$ to form C-(N-)A-S-H gel, as shown in Eqs. (4) and (5) [64–66]. Meanwhile, the extensive dissolution of GGBFS increases the concentration of Mg^{2+} in the system, which then reacts with $[Al(OH)_4]^-$ to form hydrotalcite, as shown in Eq. (6) [67]. Depending on the ratio of ABOFS to GGBFS, the composition of the hydration products varies. Specifically, when the ABOFS content is high, the $[H_3AlO_4]^{2-}$ content in the system is insufficient, and the hydration products predominantly consist of C-S-H gel and Katoite. However, as the GGBFS content increases, more C-(N-)A-S-H gel and hydrotalcite is generated. In addition, Na^+ and Al^{3+} will partially replace Si in C-S-H gel, leading to the transformation of C-S-H gel into C-(N-)A-S-H gel.

$$xCa(OH)_2 + [SiO_4]^{4-} + yH_2O \rightarrow (CaO)_x(SiO_2)(H_2O)_y + 4OH^- + (x-2)H_2O \quad (4)$$

$$Na^+ + Ca^{2+} + [H_3SiO_4]^- + [H_3AlO_4]^{2-} \rightarrow C-(N-)A-S-H \quad (5)$$

$$6Mg^{2+} + 2[Al(OH)_4]^- + CO_3^{2-} + 10OH^- + nH_2O \rightarrow Mg_6Al_2(OH)_{16}CO_3{\cdot}nH_2O \quad (6)$$

4. As the gel products continue to form, the amount of unreacted mineral phases in the system gradually decreases. Additionally, the hydration products tend to accumulate on the surface of unreacted particles, further hindering the progress of hydration, resulting in the gradually smoothed hydration rate at this stage.

3.2.7. MIP analysis

Fig. 17(a)-(c) shows the MIP results of different groups of one-part AAM pastes, including porosity, the distribution of pore sizes in various proportions, and the median pore size distribution. Fig. 17(a) exhibits that the porosity of one-part AAM pastes decreases as the GGBFS content increases, indicating the structure of pastes becomes denser, which is consistent with the micromorphology of pastes observed in Fig. 13. At 80 wt% GGBFS content, the porosity of OAAM-5 (31.01 %) was 48.8 % lower than that of OAAM-1 (63.53 %). On one hand, as shown in the TGA results, when the GGBFS content is below 60 wt%, the total amount of reaction products in one-part AAM pastes increased with the increase of GGBFS. The gel products will fill the pores in the pastes, leading to the decrease of porosity. On the other hand, GGBFS's particle size is significantly lower than BOFS, allowing it to function as a micro-aggregate and further densifying the pore structure. Thus, despite the less reaction product generated in OAAM-5 compared to OAAM-4, the porosity of OAAM-5 is still lower. Fig. 17(b) shows the proportion of different pore sizes of one-part AAM pastes. According to previous studies [68,69], the pores in AAM pastes can be classified by pore size into gel pores (0–10 nm), capillary pores (10–100 nm) and large pores (>100 nm). As mentioned above, due to the increased gel products and GGBFS's filling effect, the gel pores' proportion in one-part AAM pastes increased with the increase of GGBFS. Notably, the proportion of capillary pores in OAAM-5 is also higher than that of OAAM-4. This may be because the total amount of gel products of OAAM-5 is lower than that of OAAM-4, so the packing of gel in OAAM-5 will be looser, resulting in a rise in the proportion of capillary pores. In addition, as described in Section 3.2.5, when the GGBFS content increased to 80 wt%, the Ca ion in OAAM-5 could not completely replace the Na ion in C-(N-)A-S-H gel, which means that the proportion of N-A-S-H gel in the gel products increases. According to the study of Hu et al. [70], the porosity of N-A-S-H gel is higher than that of C-A-S-H gel, which may also be one of the reasons why the proportion of capillary pores of OAAM-5 is higher than that of OAAM-4. As displayed in Fig. 17 (c), the pore size distribution curve of one-part AAM pastes shifted progressively to the left along the X-axis with rising GGBFS content, suggesting that the median pore size of pastes decreased. This is because gel products will fill the pores with relatively large pore size, thereby reducing the overall pore size of the pores in pastes.

The compressive strength of the control groups and one-part AAM pastes at 3d and 28d are presented in Fig. 18. It can be observed that when the amounts of BOFS and ABOFS are identical, one-part AAM pastes' compressive strength is much higher than the control groups.

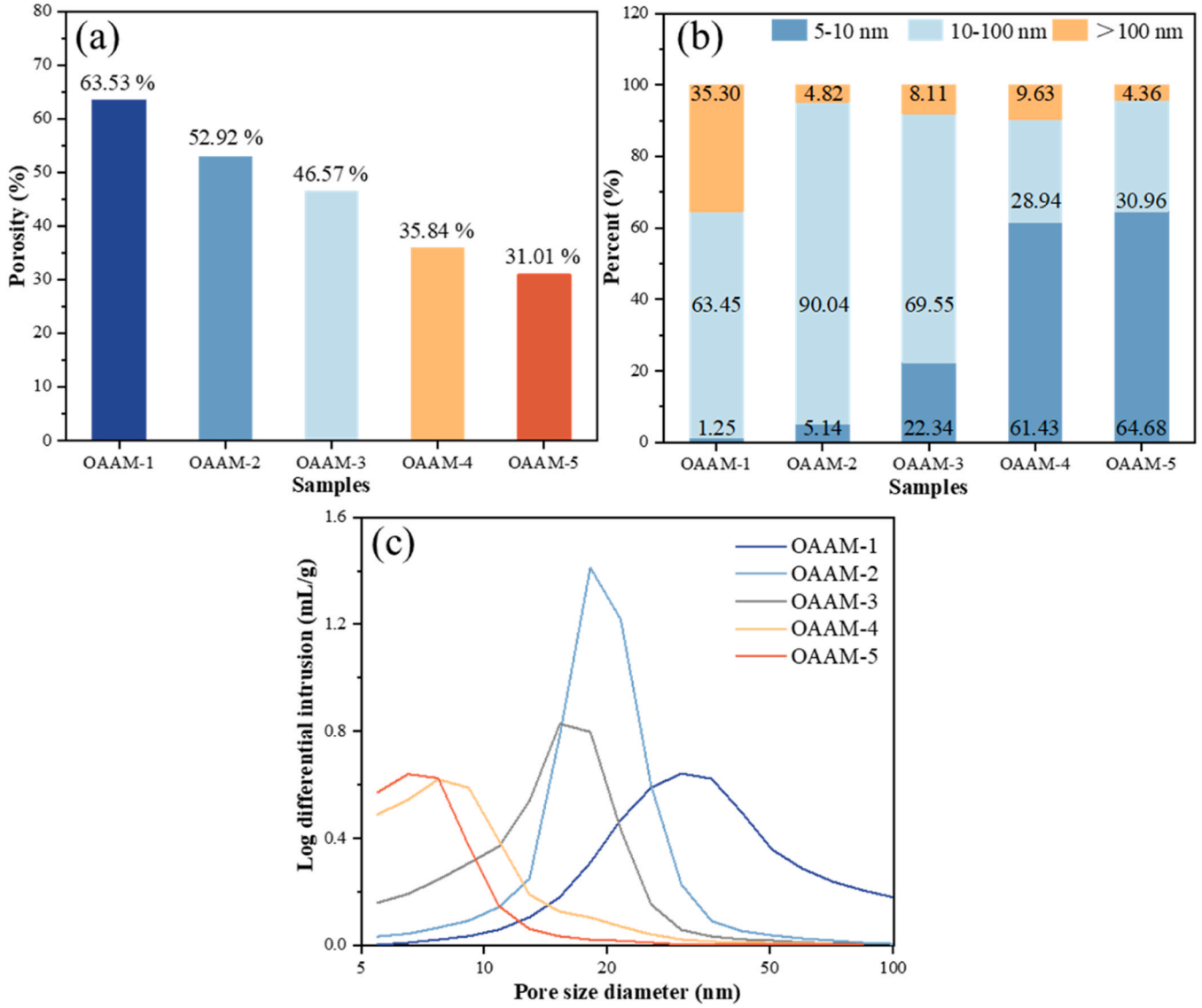

Fig. 17. Pore structure of one-part AAM pastes after curing for 28 days: (a) The cumulative porosity, (b) The proportion of different sizes of pores, and (c) The median pore size distribution.3.2.8. Compressive strength.

The 28d compressive strength of OAAM-1, OAAM-2, OAAM-3, OAAM-4 and OAAM-5 increased by 47.2 %, 23.5 %, 21.6 %, 21.4 % and 32.7 %, respectively, compared with the control groups, indicating that ABOFS has higher activity than BOFS. However, the 3d and 28d compressive strength of OAAM-1 only reached 2.7 MPa and 7.8 MPa, indicating that the activity of ABOFS is still lower than that of GGBFS. This is because that as shown in Fig. 1(b), GGBFS primarily consists of highly reactive amorphous glass phases, while BOFS has a higher content of crystalline minerals. Even after alkali activation, the content of amorphous reactive minerals in BOFS remains lower than in GGBFS. Moreover, the particle size of GGBFS is smaller, which means it has a larger specific surface area than ABOFS, allowing it to react more quickly with the alkali solution to form hydration products. Moreover, as shown in the MIP results, OAAM-1 has a high porosity (63.53 %) and a high content of large pores (35.3 %), which further reduces its compressive strength.

The compressive strength of one-part AAM pastes significantly improved with the increase of GGBFS. When the GGBFS content reached 80 wt%, the compressive strength of OAAM-5 at 3d and 28d was 20.2 MPa and 39 MPa, respectively, which was 648 % and 400 % higher than that of OAAM-1, respectively. This is because GGBFS with high reactivity can dissolve rapidly under alkaline conditions and participate in the formation of C-(N-)A-S-H gel. In addition, as mentioned above, with the increase of GGBFS, the porosity of pastes decreased and the gel pores' proportion rose. According to the study of Ma et al. [34], lower porosity and higher gel pore proportion will enhance the compressive strength of AAM materials. Therefore, the compressive strength of one-part AAM pastes increases as the GGBFS content increases. Notably, the early strength growth rate of the pastes is much higher than later strength. This is because in the early stage, the high alkalinity environment of pastes can quickly dissolve the glass phase in GGBFS and release a large amount of active silicon-aluminum monomers, thus promoting the formation of reaction products and rapidly increasing the early strength of pastes. However, as described in Section 3.2.5, the reaction rate of GGBFS in one-part AAM pastes is inhibited as the reaction proceeds, thereby limiting the growth of the later strength of pastes.

3.3. *Life cycle assessment*

Fig. 19(a) shows the ozone depletion potential (ODP) for the production of 1 kg of one-part AAM and 1 kg of OPC. It can be observed that the ODP for producing 1 kg of OPC is 3.0×10^{-8} kg CFC-11 eq, while the

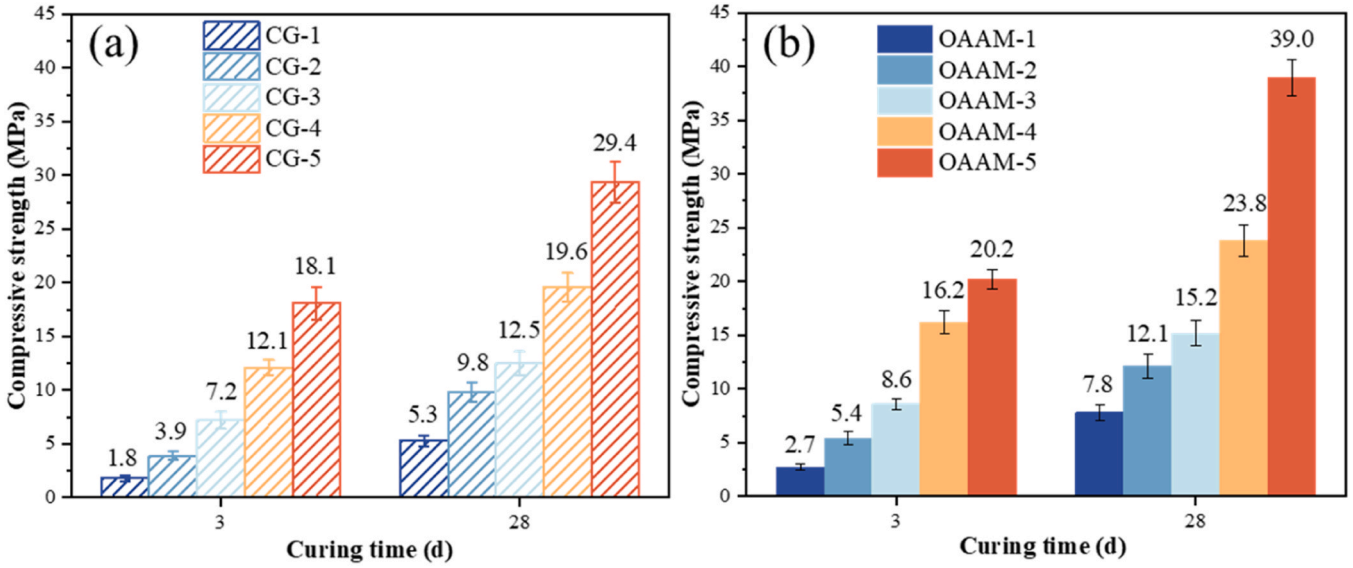

Fig. 18. Compressive strength of control groups and one-part AAM pastes curing for 3 days and 28 days, (a) Control groups, (b) One-part AAM pastes.

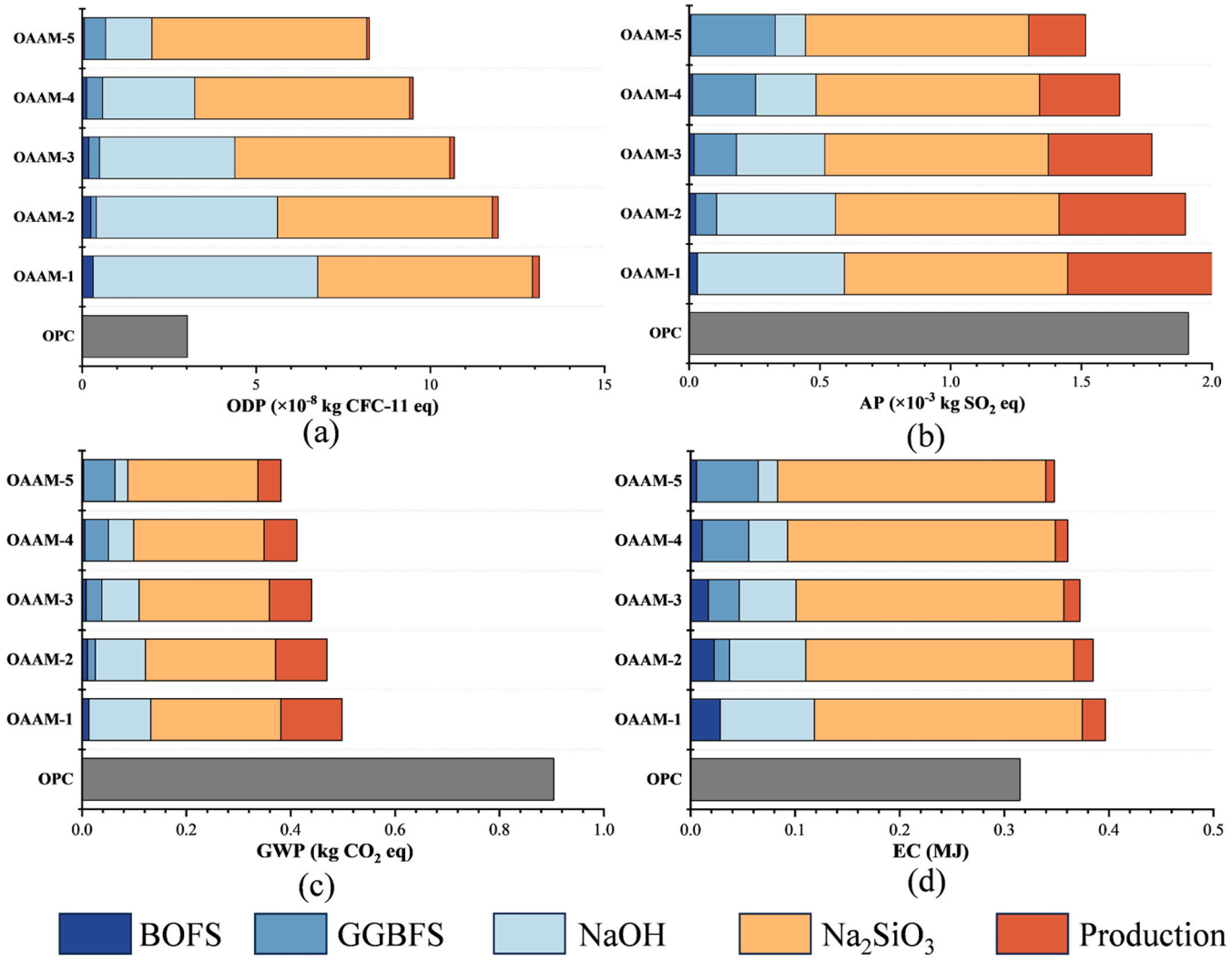

Fig. 19. The ozone depletion potential (ODP), acidification potential (AP), global warming potential (GWP) and energy consumption (EC) of OPC and one-part AAM, (a) ODP, (b) AP, (c) GWP and (d) EC.

ODP for producing 1 kg of one-part AAM ranges from 8.2×10^{-8} to 1.3×10^{-7} kg CFC-11 eq, which is 2.7–4.3 times higher than that of OPC. This is because the production of one-part AAM consumes NaOH and Na_2SiO_3, both of which contribute over 90 % to the ODP. NaOH is generated through chlor-alkali process, which releases chlorine-containing compounds into the atmosphere, thus increasing the ODP [36]. Furthermore, NaOH is also one of the raw materials for producing Na_2SiO_3, which indirectly increases the ODP of Na_2SiO_3 [71]. As a result, the ODP of one-part AAM is significantly higher than OPC.

Fig. 19(b) displays the acidification potential (AP) for the production of 1 kg of one-part AAM and 1 kg of OPC. It can be observed that the AP for producing 1 kg of OPC is 1.9×10^{-3} kg SO_2 eq, while the AP for producing 1 kg of one-part AAM ranges from 1.5×10^{-3} to 2.0×10^{-3} kg SO_2 eq. The AP of one-part AAM decreases as the content of ABOFS decreases, and when the ABOFS content in one-part AAM is below 80 wt %, the AP of one-part AAM becomes lower than that of OPC. The AP of OPC is primarily attributed to the acidic gases (such as SO_2 and NO_x) released during the clinker calcination process and fossil fuel consumption during product transportation. In contrast, the AP of one-part AAM is mainly due to the use of NaOH and Na_2SiO_3. The production of NaOH involves the electrolysis of brine, which releases chlorine and hydrogen gases that react with moisture in the atmosphere to form acidic substances. Additionally, Na_2SiO_3 is typically prepared by reacting SiO_2 with alkali at high temperatures, a process that requires significant fossil fuel consumption. Therefore, as the content of ABOFS in one-part AAM decreases, the consumption of NaOH also decreases, resulting in a reduction in AP.

Fig. 19(c) presents the global warming potential (GWP) for the production of 1 kg of one-part AAM and 1 kg of OPC. It can be observed that the GWP for producing 1 kg of OPC is 0.9 kg CO_2 eq, while the GWP for producing 1 kg of one-part AAM ranges from 0.38 to 0.50 kg CO_2 eq. The GWP of one-part AAM is reduced by 45–58 % compared to OPC, indicating that one-part AAM is a kind of low-carbon binder. This is attributed to three main factors: 1) BOFS and GGBFS are by-products of the metallurgical industry, and these materials are produced during the steelmaking process. Using them as precursors does not significantly increase CO_2 emissions. 2) The production of OPC requires the calcination of limestone at temperatures above 1400°C, a process that generates a large amount of CO_2. In contrast, ABOFS is calcined at 800 °C, and GGBFS does not require such high-temperature calcination, thus avoiding large-scale CO_2 emissions. 3) The GWP of one-part AAM is mainly attributed to the use of NaOH and Na_2SiO_3, as the production of NaOH through the chlor-alkali process and the high-temperature production of Na_2SiO_3 consume large amounts of electricity and thermal energy, increasing fossil fuel consumption and CO_2 emissions. However, despite the CO_2 emissions associated with the production of NaOH and Na_2SiO_3, their contribution to the GWP is lower compared to the calcination process in OPC production. Therefore, the overall carbon emissions of one-part AAM are significantly lower than those of OPC. To further assess the realistic potential impact of one-part AAM on reducing carbon emissions, it is essential to considered the resource availability of BOFS. China generated over 80 million tons of BOFS in 2023, according to Table 4, this quantity of BOFS could theoretically produce approximately 250 million tons of OAAM-4, assuming a 1:1 substitution ratio. This would lead to an estimated reduction of 120 million tons of CO_2 eq, based on cement's average emission factor. While this demonstrates significant carbon mitigation potential, the actual impact is limited by factors such as BOFS distribution, competing utilization, and regional logistics. Therefore, the large-scale application of one-part AAM is most promising in areas with concentrated BOFS resources and high cement demand.

Fig. 19(d) shows the energy consumption (EC) for the production of 1 kg of one-part AAM and 1 kg of OPC. It can be observed that the EC for producing 1 kg of OPC is 0.31 MJ, while the EC for producing 1 kg of one-part AAM ranges from 0.35 to 0.40 MJ. The EC of one-part AAM is 13–29 % higher than that of OPC. Similar to the GWP, the increased EC of one-part AAM is mainly attributed to the use of NaOH and Na_2SiO_3. The production of NaOH and Na_2SiO_3 involves high-energy-consuming processes such as electrolysis or high-temperature calcination, which increases overall energy consumption. Additionally, the transportation of BOFS and GGBFS over long distances also contributes to higher energy consumption. It is important to note that while OPC production also requires significant energy, the process is relatively mature, and energy efficiency is typically higher. In contrast, the production process of one-part AAM may not yet achieve the same level of energy efficiency, which could be a potential factor influencing the EC of one-part AAM.

4. Conclusions

In this study, basic oxygen furnace slag (BOFS) was pretreated by alkali fusion activation and the effect of NaOH content on the reactivity of alkali-fused basic oxygen furnace slag (ABOFS) was studied. Then, one-part alkali-activated materials (AAM) pastes were prepared using ABOFS and ground granulated blast furnace slag (GGBFS). The mechanical properties, microstructure and reaction products of one-part AAM pastes were studied, and the life cycle assessment from cradle to gate was conducted. The main findings of this study are as follows:

(1) Alkali fusion activation promoted the formation of reactive mineral phases such as C_2S, C_4AF, $C_{12}A_7$ and $NaAlO_2$ in BOFS and increased its specific surface area. The optimal NaOH content for alkali fusion activation was 10 wt%.
(2) The main reaction products of one-part AAM are C-(N-)A-S-H gel and hydrotalcite. GGBFS will promote the hydration reaction. However, when the GGBFS content exceeds 60 wt%, the accumulation of gel products and the decrease of system's alkalinity will hinder the further hydration reaction.
(3) The increase of GGBFS reduced the Ca/Si ratio and increased the Al/Si ratio of one-part AAM's matrix gel, while the Na/Si ratio showed a trend of decreasing first and then increasing. Additionally, the positive correlation between Mg/Si and Al/Si ratios indicates the formation of hydrotalcite-like phases in pastes.
(4) The pore distribution results indicate that the addition of GGBFS reduces the porosity of pastes and increases the proportion of gel pores, thereby improving its compressive strength. When the GGBFS content increased from 0 wt% to 80 wt%, the 28 d compressive strength of OAAM-5 (39 MPa) increased by 400 % compared to OAAM-1 (7.8 MPa).
(5) The global warming potential for producing 1 kg of one-part AAM is reduced by 45–58 % compared to ordinary Portland cement (OPC). However, the acidification potential, ozone depletion potential and energy consumption of one-part AAM have no advantages over OPC. While one-part AAM significantly reduces carbon emissions compared with OPC, its overall environmental impact requires further evaluation.

CRediT authorship contribution statement

Boyu Chen: Writing – review & editing, Supervision. **Dongyu Chen:** Writing – review & editing, Supervision, Methodology. **Chao Yang:** Investigation, Formal analysis. **Xinkui Yang:** Writing – original draft, Methodology, Conceptualization. **Shaopeng Wu:** Methodology, Conceptualization. **Shi Xu:** Methodology, Conceptualization. **Chen Liu:** Writing – review & editing, Investigation, Formal analysis.

Declaration of Competing Interest

The authors declare that they have no known competing financial interests or personal relationships that could have appeared to influence the work reported in this paper.

Acknowledgments

This work was supported by the National Natural Science Foundation of China (No. 52378461, No. 52208444 and No. 52068061), the project of Hebei Provincial Department of transportation (No. 202319), the Science and Technology Project of the Department of Transportation of Guangxi Autonomous Region (No. 2021-MS5–125), the Hubei Science and Technology Innovation Talent and Service Project (No. 2022EHB006) and State Key Laboratory of Silicate Materials for Architectures (Wuhan University of Technology) (SYSJJ2024-06).

Data Availability

Data will be made available on request.

References

[1] S. Yang, Z. Tang, S. Gao, L. Mo, D. Lu, Elevating carbonation efficiency and CO2 capture capacity of steel slag by sodium tripolyphosphate (STP): the role of CaCO3 morphology modification, Cem. Concr. Compos. 153 (2024) 105716.
[2] Y. Song, H. Xu, S. Wu, J. Xie, A. Chen, Y. Lv, Y. Cheng, Y. Li, High-quality utilization of reclaimed asphalt pavement (RAP) in asphalt mixture with the enhancement of steel slag and epoxy asphalt, Constr. Build. Mater. 445 (2024) 137963.
[3] C. Yang, S. Wu, J. Xie, S. Amirkhanian, Z. Zhao, H. Xu, F. Wang, L. Zhang, Development of blending model for RAP and virgin asphalt in recycled asphalt mixtures via a micron-Fe3O4 tracer, J. Clean. Prod. 383 (2023) 135407.
[4] P. Cui, S. Wu, Y. Xiao, R. Hu, T. Yang, Environmental performance and functional analysis of chip seals with recycled basic oxygen furnace slag as aggregate, J. Hazard. Mater. 405 (2021) 124441.
[5] Y. Tang, K. Schollbach, S. van der Laan, W. Chen, Activation of BOF slag with dipotassium hydrogen phosphate: enhancing hydration, carbonation resistance, and heavy metal leaching, Cem. Concr. Compos. 157 (2025) 105922.
[6] P. Cui, T. Ma, S. Wu, G. Xu, F. Wang, Texture characteristic and its enhancement mechanism in stone mastic asphalt incorporating steel slag, Constr. Build. Mater. 369 (2023) 130440.
[7] H. Xu, Y. Zou, G. Airey, H. Wang, H. Zhang, S. Wu, A. Chen, Wetting of bio-rejuvenator nanodroplets on bitumen: a molecular dynamics investigation, J. Clean. Prod. 444 (2024) 141140.
[8] C. Yang, S. Wu, P. Cui, S. Amirkhanian, Z. Zhao, F. Wang, L. Zhang, M. Wei, X. Zhou, J. Xie, Performance characterization and enhancement mechanism of recycled asphalt mixtures involving high RAP content and steel slag, J. Clean. Prod. 336 (2022) 130484.
[9] Y. Liu, Z. Zhang, G. Hou, P. Yan, Preparation of sustainable and green cement-based composite binders with high-volume steel slag powder and ultrafine blast furnace slag powder, J. Clean. Prod. 289 (2021) 125133.
[10] L. Pang, S. Liao, D. Wang, M. An, Influence of steel slag fineness on the hydration of cement-steel slag composite pastes, J. Build. Eng. 57 (2022) 104866.
[11] Y. Rui, C. Qian, CO2-fixing steel slag on hydration characteristics of cement-based materials, Constr. Build. Mater. 354 (2022) 129193.
[12] W. Li, M. Cao, F. Liu, D. Wang, J. Chang, Pretreatment of alkali activation and carbonation of steel slag for using as binding material, Cem. Concr. Compos. 149 (2024) 105521.
[13] S.K. Singh, Jyoti, P. Vashistha, Development of newer composite cement through mechano-chemical activation of steel slag, Constr. Build. Mater. 268 (2021) 121147.
[14] X. Sun, Y. Li, X. Wei, J. Yu, M. Wang, High contents of steel slag in the road concrete: Hydration mechanism, mechanical property and durability performance, Constr. Build. Mater. 400 (2023) 132703.
[15] J.L. Provis, A. Palomo, C. Shi, Advances in understanding alkali-activated materials, Cem. Concr. Res. 78 (2015) 110–125.
[16] J.L. Provis, Alkali-activated materials, Cem. Concr. Res. 114 (2018) 40–48.
[17] A. Palomo, M. Palacios, Alkali-activated cementitious materials: alternative matrices for the immobilisation of hazardous wastes: Part II. Stabilisation of chromium and lead, Cem. Concr. Res. 33 (2) (2003) 289–295.
[18] Y. Xia, Z. Liu, Z. Song, R. Zhao, J. Wu, L. Wang, J. Yan, Valorization of municipal solid waste incineration fly ash in low-carbon alkali-activated materials, Chem. Eng. J. 495 (2024) 153577.
[19] T. Schade, F. Bellmann, B. Middendorf, Quantitative analysis of C-(K)-A-S-H-amount and hydrotalcite phase content in finely ground highly alkali-activated slag/silica fume blended cementitious material, Cem. Concr. Res. 153 (2022) 106706.
[20] M.F. Alnahhal, T. Kim, A. Hajimohammadi, Distinctive rheological and temporal viscoelastic behaviour of alkali-activated fly ash/slag pastes: a comparative study with cement paste, Cem. Concr. Res. 144 (2021) 106441.
[21] R.M. Arachchige, J. Olek, F. Rajabipour, S. Peethamparan, Phase identification and micromechanical properties of non-traditional and natural pozzolan based alkali-activated materials, Constr. Build. Mater. 441 (2024) 137478.
[22] D. Huang, H. Chen, Y. Zou, Q. Yuan, H. Peng, Influence of raw material properties on microscopic and mechanical characteristics of alkali-activated materials, Case Stud. Constr. Mater. 20 (2024) e03319.
[23] R. Cai, H. Ye, Clinkerless ultra-high strength concrete based on alkali-activated slag at high temperatures, Cem. Concr. Res. 145 (2021) 106465.
[24] M. Liu, Y. Zhang, C. Wang, Z. Ma, Reusing thermoactivated waste paste/concrete powder for sustainable alkali-activated materials: effects of thermoactivated temperature, Constr. Build. Mater. 437 (2024) 136973.
[25] W. Wu, Y. Li, X. Du, H. Zhao, J. Kong, L. Wang, M. Chen, H. Quan, Formulation and characterization of one-part Ca-based alkali-activated slag-steel slag materials, Constr. Build. Mater. 449 (2024) 138432.
[26] C. Xu, H. Jing, F. Liu, Z. Zhang, The multi-objective optimization and mix parameter evaluation of one-part alkali-activated grouting material, J. Clean. Prod. 448 (2024) 141638.
[27] T. Luukkonen, Z. Abdollahnejad, J. Yliniemi, P. Kinnunen, M. Illikainen, One-part alkali-activated materials: a review, Cem. Concr. Res. 103 (2018) 21–34.
[28] Z. Yang, W. Tang, D. Zhang, J. Zhang, K. Wang, Z. Zhao, Hydration mechanism of alkali-activated cementitious materials entirely prepared by solid wastes, J. Build. Eng. 97 (2024) 110921.
[29] K. Luo, W. Zhang, J. Ye, J. Chen, F. Yan, X. Ren, J. Li, Mechanism of Na2CO3 on early properties of red mud-based alkali-activated cementitious materials, Constr. Build. Mater. 449 (2024) 138369.
[30] X. Zhu, W. Li, Z. Du, S. Zhou, Y. Zhang, F. Li, Recycling and utilization assessment of steel slag in metakaolin based geopolymer from steel slag by-product to green geopolymer, Constr. Build. Mater. 305 (2021) 124654.
[31] L. Zhang, Y. Zhang, Q. Wang, W. Zhang, Z. Li, Sustainable alkali-activated materials: Leveraging spontaneous combustion coal gangue for enhanced cementitious performance, Materials Today, Communications 41 (2024) 111044.
[32] N. Ye, J. Yang, S. Liang, Y. Hu, J. Hu, B. Xiao, Q. Huang, Synthesis and strength optimization of one-part geopolymer based on red mud, Constr. Build. Mater. 111 (may15) (2016) 317–325.
[33] A. Adesina, Synthesis, characterization, and efficacy of alkali-activated materials from mine tailings: a review, Waste Manag. 191 (2025) 23–46.
[34] C. Ma, B. Zhao, L. Wang, G. Long, Y. Xie, Clean and low-alkalinity one-part geopolymeric cement: effects of sodium sulfate on microstructure and properties, J. Clean. Prod. 252 (2020) 119279.
[35] Y. Yang, J. Zhang, Y. Fu, W. Long, B. Dong, Synthesis of one-part geopolymers from alkaline-activated molybdenum tailings: mechanical properties and microstructural evolution, J. Clean. Prod. 443 (2024) 141129.
[36] L. Imtiaz, S. Kashif-ur-Rehman, W.S. Alaloul, K. Nazir, M.F. Javed, F. Aslam, M. A. Musarat, Life cycle impact assessment of recycled aggregate concrete, geopolymer concrete, and recycled aggregate-based geopolymer concrete, Sustainability 13 (24) (2021) 13515.
[37] A. Hajimohammadi, J.S.J. van Deventer, Characterisation of one-part geopolymer binders made from fly ash, Waste Biomass. Valoriz. 8 (1) (2017) 225–233.
[38] X. Luo, L. Huang, L. Wei, M. Chen, Z. Zhou, T. Zhang, A technique for preparing one-part geopolymers by activating alkali-fused lithium slag with solid sodium silicate, Constr. Build. Mater. 435 (2024) 136817.
[39] C. Ma, G. Long, Y. Shi, Y. Xie, Preparation of cleaner one-part geopolymer by investigating different types of commercial sodium metasilicate in China, J. Clean. Prod. 201 (2018) 636–647.
[40] J. Yang, H. Bai, X. He, J. Zeng, Y. Su, X. Wang, H. Zhao, C. Mao, Performances and microstructure of one-part fly ash geopolymer activated by calcium carbide slag and sodium metasilicate powder, Constr. Build. Mater. 367 (2023) 130303.
[41] B. Ma, Z. Zhu, W. Huo, L. Yang, Y. Zhang, H. Sun, X. Zhang, Assessing the viability of a high performance one-part geopolymer made from fly ash and GGBS at ambient temperature, J. Build. Eng. 75 (2023) 106978.
[42] N. Ye, Y. Chen, J. Yang, S. Liang, Y. Hu, J. Hu, S. Zhu, W. Fan, B. Xiao, Transformations of Na, Al, Si and Fe species in red mud during synthesis of one-part geopolymers, Cem. Concr. Res. 101 (2017) 123–130.
[43] C. Chen, S. Shenoy, Y. Pan, K. Sasaki, Q. Tian, H. Zhang, Mechanical activation of coal gasification slag for one-part geopolymer synthesis by alkali fusion and component additive method, Constr. Build. Mater. 411 (2024) 134585.
[44] D.L.Y. Kong, J.G. Sanjayan, Effect of elevated temperatures on geopolymer paste, mortar and concrete, Cem. Concr. Res. 40 (2) (2010) 334–339.
[45] S. Saha, C. Rajasekaran, Enhancement of the properties of fly ash based geopolymer paste by incorporating ground granulated blast furnace slag, Constr. Build. Mater. 146 (2017) 615–620.
[46] ISO, ISO 14040: 2006. Environmental management—Life cycle assessment—Principles and framework. International Organization for Standardization, Geneva (2006).
[47] Z. Ghouleh, Y. Shao, S. Zhang, Performance of eco-concrete made from waste-derived eco-cement, J. Clean. Prod. 289 (2021) 125758.
[48] Y. Zhao, P. Wu, J. Qiu, Z. Guo, Y. Tian, X. Sun, X. Gu, Recycling hazardous steel slag after thermal treatment to produce a binder for cemented paste backfill, Powder Technol. 395 (2022) 652–662.
[49] S. Song, H.M. Jennings, Pore solution chemistry of alkali-activated ground granulated blast-furnace slag11This paper was originally submitted to Advanced Cement Based Materials. The paper was received at the Editorial Office of Cement and Concrete Research on 12 November 1998 and accepted in final form on 16 November 1998, Cem. Concr. Res. 29 (2) (1999) 159–170.
[50] C. Liu, Z. Li, S. Nie, J. Skibsted, G. Ye, Structural evolution of calcium sodium aluminosilicate hydrate (C-(N-)A-S-H) gels induced by water exposure: the impact of Na leaching, Cem. Concr. Res. 178 (2024) 107432.
[51] R. Myers, S.A. Bernal, J. Gehman, J. Provis, The Role of Al in Cross-Linking of Alkali-Activated Slag Cements, (2014).
[52] O. Burciaga-Diaz, J.I. Escalante-Garcia, Structure, mechanisms of reaction, and strength of an alkali-activated blast-furnace slag, J. Am. Ceram. Soc. 96 (12) (2013) 3939–3948.

[53] E. Kapeluszna, Ł. Kotwica, A. Różycka, Ł. Gołek, Incorporation of Al in C-A-S-H gels with various Ca/Si and Al/Si ratio: Microstructural and structural characteristics with DTA/TG, XRD, FTIR and TEM analysis, Constr. Build. Mater. 155 (2017) 643–653.
[54] C. Liu, X. Liang, Y. Chen, Z. Li, G. Ye, Degradation of alkali-activated slag subjected to water immersion, Cem. Concr. Compos. 142 (2023) 105157.
[55] E. Bernard, Y. Yan, B. Lothenbach, Effective cation exchange capacity of calcium silicate hydrates (C-S-H), Cem. Concr. Res. 143 (2021) 106393.
[56] A. Vidmer, G. Sclauzero, A. Pasquarello, Infrared spectra of jennite and tobermorite from first-principles, Cem. Concr. Res. 60 (2014) 11–23.
[57] M.B. Haha, G.L. Saout, F. Winnefeld, B. Lothenbach, Influence of activator type on hydration kinetics, hydrate assemblage and microstructural development of alkali activated blast-furnace slags, Cem. Concr. Res. 41 (3) (2011) 301–310.
[58] E. Kanezaki, Thermal behavior of the hydrotalcite-like layered structure of Mg and Al-layered double hydroxides with interlayer carbonate by means of in situ powder HTXRD and DTA/TG, Solid State Ion. 106 (3) (1998) 279–284.
[59] K. Rozov, U. Berner, C. Taviot-Gueho, F. Leroux, G. Renaudin, D. Kulik, L. W. Diamond, Synthesis and characterization of the LDH hydrotalcite–pyroaurite solid-solution series, Cem. Concr. Res. 40 (8) (2010) 1248–1254.
[60] G. Villain, M. Thiery, G. Platret, Measurement methods of carbonation profiles in concrete: thermogravimetry, chemical analysis and gammadensimetry, Cem. Concr. Res. 37 (8) (2007) 1182–1192.
[61] M.B. Haha, B. Lothenbach, G.L. Saout, F. Winnefeld, Influence of slag chemistry on the hydration of alkali-activated blast-furnace slag — part I: effect of MgO, Cem. Concr. Res. 41 (9) (2011) 955–963.
[62] I.G. Richardson, Tobermorite/jennite- and tobermorite/calcium hydroxide-based models for the structure of C-S-H: applicability to hardened pastes of tricalcium silicate, β-dicalcium silicate, Portland cement, and blends of Portland cement with blast-furnace slag, metakaolin, or silica fume, Cem. Concr. Res. 34 (9) (2004) 1733–1777.
[63] C. Xu, W. Ni, K. Li, S. Zhang, Y. Li, D. Xu, Hydration mechanism and orthogonal optimisation of mix proportion for steel slag–slag-based clinker-free prefabricated concrete, Constr. Build. Mater. 228 (2019) 117036.
[64] J. Zhao, Z. Li, D. Wang, P. Yan, L. Luo, H. Zhang, H. Zhang, X. Gu, Hydration superposition effect and mechanism of steel slag powder and granulated blast furnace slag powder, Constr. Build. Mater. 366 (2023) 130101.
[65] J. Zhao, Z. Li, H. Zhu, Q. Liu, J. Liu, Dissolution-precipitation hydration mechanism of steel slag based on ion exchange of a layered alkali-activator, Constr. Build. Mater. 411 (2024) 134795.
[66] J. Liu, J. Zhao, J. Liang, Exploring properties and hydration mechanisms in clinker-free cement formulated from steel industry solid waste using the extreme vertices method, Compos. Part B Eng. 291 (2025) 112018.
[67] Y. Shi, Q. Zhao, C. Xue, Y. Jia, W. Guo, Y. Zhang, Y. Qiu, Preparation and curing method of red mud-calcium carbide slag synergistically activated fly ash-ground granulated blast furnace slag based eco-friendly geopolymer, Cem. Concr. Compos. 139 (2023) 104999.
[68] A.C.A. Muller, Characterization of porosity & CSH in cement pastes by ^{1}H NMR, Epfl, 2014.
[69] X. Shi, P. Yang, L. Li, X. Geng, X. Liu, J. Zhao, Strength and microscopic pore structure characterization of cement-fly ash stabilized organic soil under freeze-thaw cycles, Constr. Build. Mater. 420 (2024) 135635.
[70] X. Hu, C. Shi, Z. Shi, L. Zhang, Compressive strength, pore structure and chloride transport properties of alkali-activated slag/fly ash mortars, Cem. Concr. Compos. 104 (2019) 103392.
[71] D.A. Salas, A.D. Ramirez, N. Ulloa, H. Baykara, A.J. Boero, Life cycle assessment of geopolymer concrete, Constr. Build. Mater. 190 (2018) 170–177.